

An inhibitor of oxidative phosphorylation exploits cancer vulnerability

Jennifer R. Molina^{1,2,16}, Yuting Sun^{1,2,16}, Marina Protopopova^{1,2}, Sonal Gera^{1,2}, Madhavi Bandi^{1,2}, Christopher Bristow^{1,2}, Timothy McAfoos¹, Pietro Morlacchi^{1,15}, Jeffrey Ackroyd³, Ahmed-Noor A. Agip⁴, Gheath Al-Atrash⁵, John Asara⁶, Jennifer Bardenhagen¹, Caroline C. Carrillo⁷, Christopher Carroll¹, Edward Chang^{1,2}, Stefan Ciurea⁵, Jason B. Cross¹, Barbara Czako¹, Angela Deem^{1,2}, Naval Daver⁸, John Frederick de Groot⁷, Jian-Wen Dong⁷, Ningping Feng^{1,2}, Guang Gao^{1,2}, Jason Gay^{1,2}, Mary Geck Do¹, Jennifer Greer¹, Virginia Giuliani^{1,2}, Jing Han^{1,2}, Lina Han⁸, Verlene K. Henry⁷, Judy Hirst⁴, Sha Huang¹, Yongying Jiang¹, Zhijun Kang¹, Tin Khor^{1,2}, Sergej Konoplev⁹, Yu-Hsi Lin³, Gang Liu¹, Alessia Lodi¹⁰, Timothy Lofton¹, Helen Ma⁸, Mikhila Mahendra^{1,2}, Polina Matre⁸, Robert Mullinax^{1,2}, Michael Peoples^{1,2}, Alessia Petrocchi¹, Jaime Rodriguez-Canale¹¹, Riccardo Serreli⁴, Thomas Shi^{1,2}, Melinda Smith^{1,2}, Yoko Tabe^{8,12}, Jay Theroff¹, Stefano Tiziani¹⁰, Quanyun Xu¹, Qi Zhang⁸, Florian Muller³, Ronald A. DePinho¹³, Carlo Toniatti^{1,2}, Giulio F. Draetta^{1,2,14}, Timothy P. Heffernan^{1,2}, Marina Konopleva⁸, Philip Jones^{1,16}, M. Emilia Di Francesco^{1,16} and Joseph R. Marszalek^{1,2,16*}

Metabolic reprogramming is an emerging hallmark of tumor biology and an actively pursued opportunity in discovery of oncology drugs. Extensive efforts have focused on therapeutic targeting of glycolysis, whereas drugging mitochondrial oxidative phosphorylation (OXPHOS) has remained largely unexplored, partly owing to an incomplete understanding of tumor contexts in which OXPHOS is essential. Here, we report the discovery of IACS-010759, a clinical-grade small-molecule inhibitor of complex I of the mitochondrial electron transport chain. Treatment with IACS-010759 robustly inhibited proliferation and induced apoptosis in models of brain cancer and acute myeloid leukemia (AML) reliant on OXPHOS, likely owing to a combination of energy depletion and reduced aspartate production that leads to impaired nucleotide biosynthesis. In models of brain cancer and AML, tumor growth was potently inhibited in vivo following IACS-010759 treatment at well-tolerated doses. IACS-010759 is currently being evaluated in phase 1 clinical trials in relapsed/refractory AML and solid tumors.

Metabolic reprogramming is a well-appreciated hallmark of cancer, and there has been extensive drug discovery research in this area. Coordinated upregulation of glycolysis, known as the Warburg effect¹, is a phenomenon that arises as tumor cells adapt to increased demands for energy and biomass production. Elevated glycolysis is currently being clinically exploited using positron emission tomography with 2-deoxy-2-fluoro-D-glucose (FDG-PET) to detect metabolically active tumors²; it is also being therapeutically exploited through the development of inhibitors of enzymes essential for glucose metabolism³. Recent reports

emphasize that, in addition to a strong dependence on glycolysis, many tumors or cancer cell subpopulations rely on OXPHOS⁴ for bioenergetic^{5–15} and biosynthetic processes^{16,17}. Biguanides, such as metformin, have been evaluated for the treatment of diabetes and metabolic disorders, providing rationale that targeting OXPHOS for clinical benefit can be done safely. However, metformin and other drugs targeting oxidative metabolism possess pharmacological limitations, including inadequate potency (i.e., biguanides)^{18,19}, transport-mediated accumulation (i.e., OCT1 for metformin)²⁰, ‘off-target’ pharmacology (i.e., rotenone)²¹, or lack of a suitable

¹Institute for Applied Cancer Science, University of Texas MD Anderson Cancer Center, Houston, TX, USA. ²Center for Co-Clinical Trials, University of Texas MD Anderson Cancer Center, Houston, TX, USA. ³Department of Cancer Imaging Systems, University of Texas MD Cancer Center, Houston, TX, USA. ⁴Medical Research Council Mitochondrial Biology Unit, University of Cambridge, Wellcome Trust/MRC Building, Cambridge Biomedical Campus, Cambridge, UK. ⁵Department of Stem Cell Transplantation and Cellular Therapy, University of Texas MD Anderson Cancer Center, Houston, TX, USA. ⁶Beth Israel Deaconess Medical Center, Harvard Medical School, Boston, MA, USA. ⁷Department of Neuro-Oncology, University of Texas MD Anderson Cancer Center, Houston, TX, USA. ⁸Department of Leukemia, University of Texas MD Anderson Cancer Center, Houston, TX, USA. ⁹Department of Hematopathology, University of Texas MD Anderson Cancer Center, Houston, TX, USA. ¹⁰Department of Nutritional Sciences, University of Texas at Austin, Austin, TX, USA. ¹¹Department of Translational Molecular Pathology, University of Texas MD Anderson Cancer Center, Houston, TX, USA. ¹²Department of Next Generation Hematology Laboratory Medicine, Department of Laboratory Medicine, Juntendo University School of Medicine, Tokyo, Japan. ¹³Department of Cancer Biology, University of Texas MD Anderson Cancer Center, Houston, TX, USA. ¹⁴Department of Genomic Medicine, University of Texas MD Anderson Cancer Center, Houston, TX, USA. ¹⁵Present address: Agilent Technologies Inc., Lexington, MA, USA. ¹⁶These authors contributed equally: Jennifer R. Molina, Yuting Sun, Philip Jones, M. Emilia Di Francesco, Joseph R. Marszalek. *e-mail: jrmarszalek@mdanderson.org

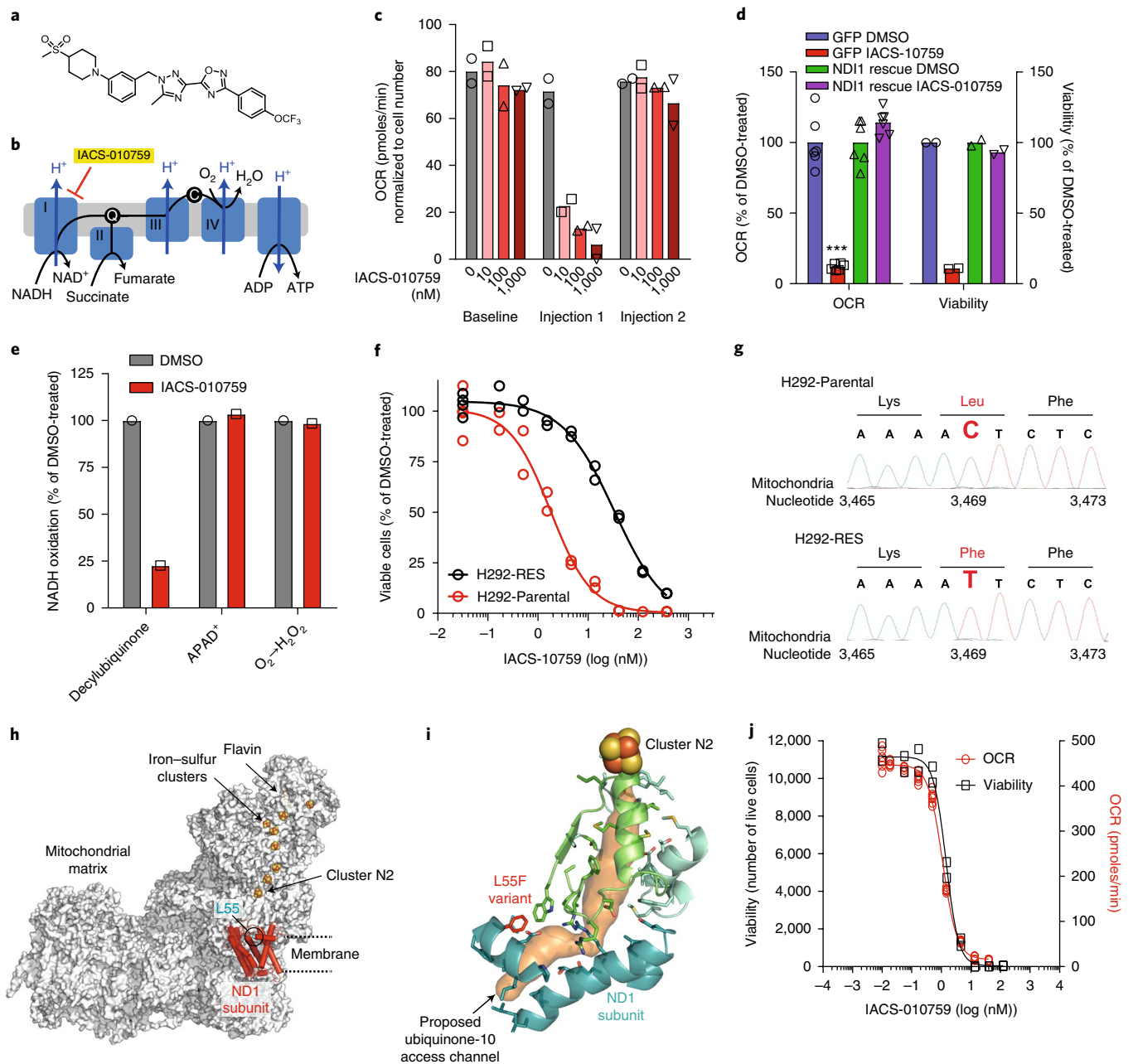


Fig. 1 | IACS-010759 is a potent inhibitor of mitochondria complex I. **a**, The structure of IACS-010759. **b**, An illustration of the mitochondria electron transport chain. **c**, The OCR of permeabilized H460 cells grown in medium supplemented with pyruvate and malate to measure complex I activity that were then treated with IACS-010759 (Injection 1) and 10 mM succinate (Injection 2) (mean from $n=2$ cultures plotted, performed one time). **d**, OCR of H460 cells engineered to ectopically express *Saccharomyces cerevisiae* NDI1 (complex I equivalent) or GFP grown in Seahorse medium (mean from $n=6$ cultures plotted, data shown are from 1 representative experiment out of 2 experiments) and relative viability (cell confluence) in galactose medium (mean from $n=2$ cultures plotted, performed one time) following treatment with either DMSO or 14 nM IACS-010759 for 1 h (for OCR) or 72 h (for viability). *** $P < 0.0001$ by two-sided Student's t -test. **e**, Complex I isolated from mouse mitochondria was treated with 60 nM IACS-010759 to measure effects on ubiquinone reduction (decylubiquinone) (mean from $n=9$ technical replicates plotted), flavin site activity as determined via 3-acetylpyridine adenine dinucleotide (APAD⁺) expression (mean from $n=3$ technical replicates plotted), and H₂O₂ production (mean from $n=3$ technical replicates plotted). Results with IACS-010759 are normalized to those from DMSO treatment. **f**, Dose-response curves for a H292-Parental cell line and an H292 clone resistant to IACS-010759 (H292-RES) (mean from $n=2$ cultures plotted, performed 1 time). **g**, Sanger sequencing chromatogram of PCR-amplified *MT-ND1* DNA from an H292-RES cell resistant to IACS-010759. **h**, The structure of complex I with the location of the ND1 subunit highlighted in red. **i**, The location of the L55F mutation relative to the proposed ubiquinone-binding channel (shown as a surface) in complex I. Residues and structures that form the binding site are shown; the redox-active ubiquinone headgroup moves through the channel and is reduced next to cluster N2. **h** and **i** were created using the highly homologous structure of bovine complex I (5LC5.pdb)²⁹. **j**, H460 cells were treated with IACS-010759, and OCR (mean from $n=6$ cultures plotted) and viability (mean from $n=2$ cultures plotted) were measured after 1 or 72 h, respectively. **c**, **d**, and **j** were repeated once; **e** and **f** were repeated ≥ 2 times, and each replicate had comparable results.

pharmacokinetic (PK) profile (i.e., oligomycin), that restrict their use as oncology therapeutics. Here, we report the discovery of IACS-010759 (Fig. 1a), a clinical-grade, highly potent and selective small-molecule inhibitor of complex I of the mitochondrial electron transport chain (ETC; Fig. 1b) and its mechanism of antitumor activity in acute myeloid leukemia (AML) and genetically defined subsets of glioblastoma and neuroblastoma.

Results

IACS-010759 was identified through an extensive medicinal chemistry campaign of lead optimization initially seeded with known modulators of Hypoxia-inducible factor 1- α (HIF-1 α) that act via inhibition of OXPHOS^{22–24}. Consistent with IACS-010759 acting solely at complex I, treatment of detergent-permeabilized cells with IACS-010759 in medium supplemented with pyruvate and malate (to generate NADH for use by complex I) resulted in an attenuated oxygen consumption rate (OCR; Fig. 1c), whereas the OCR was not affected by treatment with IACS-010759 when medium was supplemented with succinate to feed complex II, thus bypassing the requirement for complex I function. This mechanism was further supported by the finding that ectopic expression of *Saccharomyces cerevisiae* NDI1, the yeast complex I ortholog^{25,26}, completely restored cell viability and OCR to baseline levels in the presence of IACS-010759 (Fig. 1d and Supplementary Fig. 1a,b). Similar results were obtained with rotenone, a well-established but less-specific inhibitor of complex I (Supplementary Fig. 1c); however, only a partial rescue of viability was observed, likely because of off-target toxicity (Supplementary Figs. 2b,d,g,i,j,l). Further, IACS-010759 treatment of complex I isolated from mouse mitochondria resulted in decreased catalysis owing to inhibition at the ubiquinone-binding site versus the flavin site, with no effect on H₂O₂ generation (Fig. 1e). To define the interaction of IACS-010759 with complex I, clones with reduced sensitivity to IACS-010759 were generated by growing cells for 12 weeks in the presence of increasing amounts of IACS-010759 in galactose medium, wherein cells were rendered dependent on OXPHOS for survival^{27,28}. Half-maximal inhibitory concentration (IC₅₀) values for resistant clones ranged from 3.7 to 74 nM as compared to 1.1 nM for parental cells (Supplementary Fig. 1d). In contrast to IACS-010759, sensitivity to rotenone was consistent in most clones (Supplementary Fig. 1d), indicating that the reduced sensitivity to IACS-010759 was not likely due to a general decrease in complex I dependence (see Fig. 1f for representative dose-response curves for clone DC4 and the parental cell line). Total and mitochondrial RNA from 12 clones were subjected to next-generation sequencing, which confirmed that 9 of the clones contained an identical nucleotide change (m.C3469T) in their mitochondrial DNA (mtDNA) yielding an amino acid substitution (p.L55F) in the ND1 subunit of complex I (Fig. 1g). This residue resides close to the entrance of the proposed ubiquinone-10 binding channel of complex I (Fig. 1h,i)²⁹, but numerous attempts to ectopically express mutant ND1-L55F through multiple strategies were unsuccessful owing to the technical challenges of ectopically expressing proteins encoded by mtDNA. Taken together, these data are consistent with IACS-010759 binding in or at the entrance to the ubiquinone channel and thus blocking ubiquinone binding or function to inhibit complex I activity.

To correlate phenotypic response directly with OXPHOS inhibition, the effect of IACS-010759 on the OCR of cells grown in Seahorse medium was compared to the viability of cells grown in galactose-containing medium. IACS-010759 robustly inhibited both OCR and galactose-dependent cell viability and had nearly identical IC₅₀ values of 1.4 nM in both assays (Fig. 1j). By comparison, IC₅₀ values for rotenone were 0.24 nM and 0.87 nM in assays for OCR and galactose-dependent cell viability, respectively (Supplementary Fig. 1e). IC₅₀ values in these assays were similar for both IACS-010759 and for rotenone across several human cell line models

(Supplementary Table 1). To examine the potency of IACS-010759 across species that are widely used for preclinical safety analysis, the response of representative cell lines from mouse, rat, dog, and cynomolgus monkey to the inhibitor was assessed using the highly quantitative galactose growth assay. IACS-010759 was similarly active in mouse (average IC₅₀ = 5.6 nM), rat (IC₅₀ = 12.2 nM), and cynomolgus monkey (IC₅₀ = 8.7 nM), thus making them appropriate preclinical models for further safety studies (Supplementary Table 1). In contrast, IACS-010759 was minimally active in canine cell lines (IC₅₀ = 180–360 nM). Rotenone potency was very similar across all species (Supplementary Table 1).

The effect of IACS-010759 on cell growth and viability was evaluated across a panel of cancer cell lines and normal diploid cells using standard culture medium containing glucose and glutamine, which provides multiple energy sources to the cells. IACS-010759 yielded a maximal reduction of growth of > 50% in the majority of cancer cell lines (24 of 30 pancreatic (PDAC), 19 of 20 ovarian, 13 of 16 triple-negative breast (TNBC), 8 of 10 non-small-cell lung (NSCLC)) and a subset (11 of 30 PDAC, 10 of 20 ovarian, 5 of 16 TNBC, 2 of 10 NSCLC) exhibited > 100% growth inhibition (Supplementary Fig. 3a–d). All diploid cell lines were insensitive to IACS-010759 and exhibited little or no growth inhibition (Supplementary Fig. 2a,c,g,i,k), whereas rotenone exposure reduced viability in these models, consistent with rotenone possessing nonspecific off-target toxicities (Supplementary Fig. 2b,d,h,j,l). These data establish differential sensitivity of normal and cancer cells to OXPHOS inhibition by IACS-010759.

In addition to its direct antigrowth effects, OXPHOS inhibition has been reported to reduce hypoxia and HIF pathway activity^{4,22,24,30}. In accordance with this notion, exposure of cell line spheres to IACS-010759 eliminated hypoxia, most likely as a consequence of increased intracellular oxygen (Supplementary Fig. 4a,b). This coincided with decreased HIF pathway activity (Supplementary Fig. 4c) via oxygen-, prolyl hydroxylase- and VHL-dependent degradation of HIF-1 α (Supplementary Fig. 4d–h).

IACS-010759 targets glycolysis-deficient tumor cells. Glycolysis is under negative control by OXPHOS and is induced by tricarboxylic acid cycle (TCA)-mediated allosteric inhibition of glycolytic enzymes (the ‘Pasteur effect’³¹); therefore, genetic or pharmacological OXPHOS inhibition should result in compensatory upregulation of glycolysis to maintain ATP levels and redox balance, resulting in modest antiproliferation effects³². Thus, we hypothesized that tumor cells with a reduced capacity for compensatory glycolysis would be more sensitive to OXPHOS inhibition.

As previously reported, a subpopulation of brain tumor cell lines with homozygous deletion of Enolase 1 (*ENO1*) are glycolysis-deficient owing to a > 90% reduction of cellular enolase enzymatic activity^{33,34}. Consistent with glycolysis inhibition at the step of enolase enzymatic activity, the levels of glycolysis metabolites upstream of enolase were elevated in *ENO1*-null cell lines, such as D423 and Gli56, whereas metabolites downstream of enolase were reduced relative to glioblastoma multiforme (GBM) cell lines with a heterozygous *ENO1* mutation or wild-type *ENO1* (Supplementary Fig. 5a). Ectopic expression of wild-type *ENO1* in Gli56 and D423 (Supplementary Fig. 5b) robustly increased lactate production, consistent with restoration of glycolysis (Fig. 2a and Supplementary Fig. 5c). Further, there was minimal lactate production upon treatment of parental Gli56 cells with IACS-010759, whereas the baseline level and induction of lactate production were substantially increased in Gli56 cells ectopically expressing *ENO1* (Supplementary Fig. 5d). Similar to *ENO1*-null cells, phosphoglycerate dehydrogenases (PGD)-null cells, such as the NB1 cell line, are glycolysis-deficient, as these cells accumulate 6-phosphogluconate, an allosteric inhibitor of glucose-6-phosphate isomerase^{35–37}. We evaluated the metabolic profile of NB1 cells by determining the extracellular

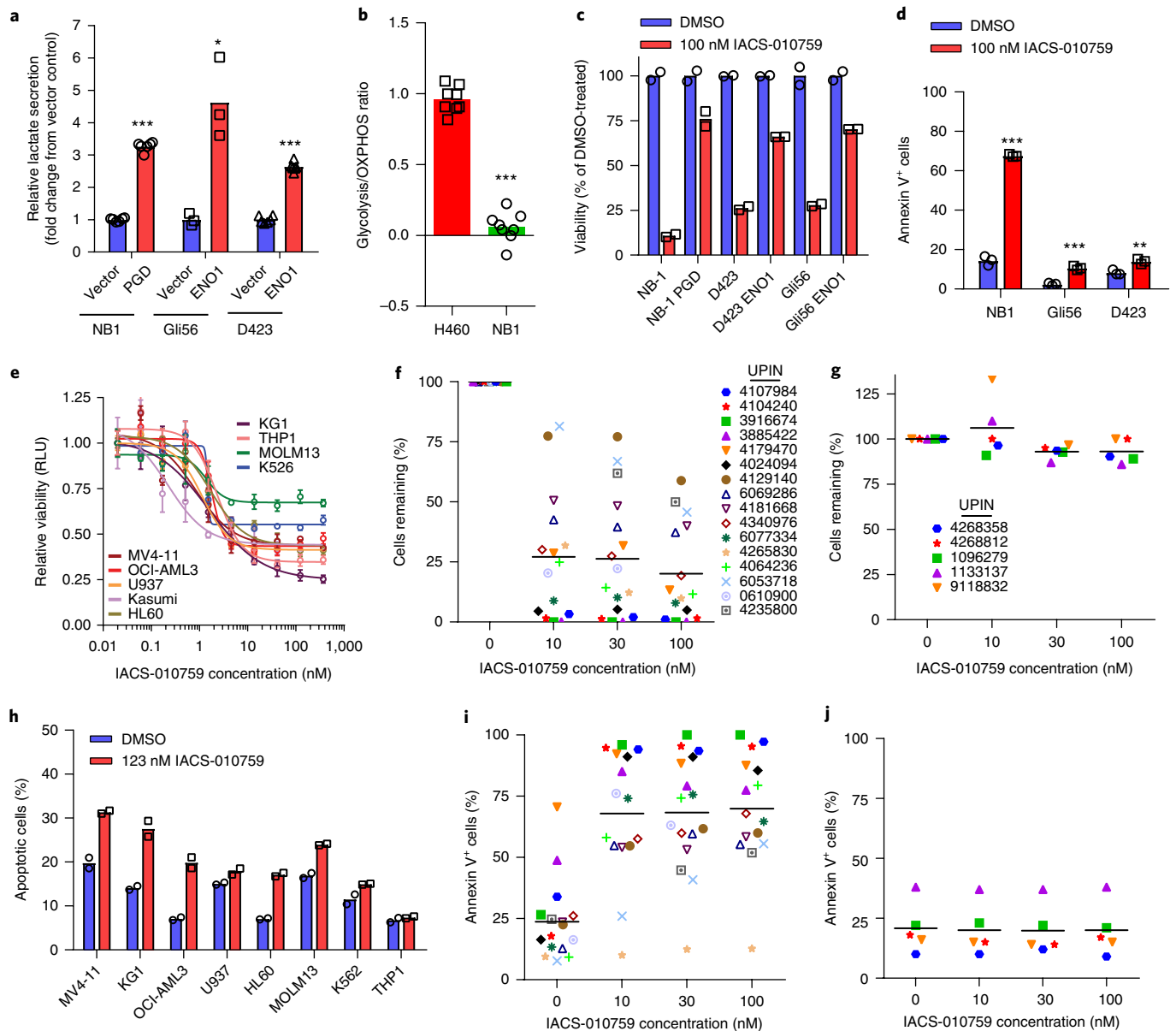


Fig. 2 | Glycolysis-deficient and AML tumor cells are sensitive to OXPPOS inhibition. **a**, Extracellular lactate levels (indicating glycolysis endpoint) in NB1 (*PGD* (*6PGD*)^{-/-}), Gli56 (*ENO1*^{-/-}), and D423 (*ENO1*^{-/-}) cells and their counterparts that were each engineered to ectopically express either PGD (NB1) or ENO1 (Gli56 and D423). The mean and individual data points for $n=6$ cultures for NB1 and D423 and $n=3$ cultures for Gli56 are plotted. For each cell line, the vector control was defined as 1. **b**, Results from Seahorse analysis measuring the ratio of glycolysis (proton production rate) to OXPPOS (OCR) in NB1 cells and H460 cells (mean and individual data points for $n=8$ cultures are plotted). **c**, Percent change in viability of the same matched-pair cell lines as in **a** that were cultured for 3 d in medium containing 100 nM IACS-010759 (mean and individual data points for $n=2$ cultures for NB1 and D423; $n=3$ cultures for Gli56 are plotted) relative to cells treated with DMSO. **d**, Percentage of annexin V⁺ NB1, Gli56, and D423 cells cultured in medium containing DMSO or 100 nM IACS-010759 for 3 d (mean and individual data points for $n=3$ cultures are plotted). **e**, Viability of AML cell lines treated with indicated concentrations of IACS-010759 for 3–7 d. Data represent mean \pm s.d. from $n=3$ cultures. **f, g**, Viability of primary AML (**f**) or normal bone marrow (**g**) samples treated ex vivo with 0, 10, 30, or 100 nM IACS-010759 for 4 or 5 d. Data from IACS-010759-treated samples were normalized to corresponding DMSO-treated controls. **h**, Percentage of apoptotic cells (propidium iodide (PI)⁺ and annexin V⁺) for each AML cell line (mean and individual data points for $n=2$ cultures are plotted; a replicate study was performed only for OCI-AML3 with comparable results) after culture for 72 h in medium containing DMSO or 123 nM IACS-010759. **i, j**, Percentage of apoptotic (annexin V⁺) cells in primary AML (**i**) or normal bone marrow (**j**) cells after culture for 4 or 5 d in medium containing DMSO or IACS-010759. For **f, g, i, and j**, each point is the mean of three cultures from a single patient sample analyzed in one experiment; the bars represent the mean value for all of the samples. Patient sample (UPIN) characteristics are included in Supplementary Table 2. *** $P < 0.0001$, ** $P < 0.001$, * $P < 0.05$ by two-sided Student's *t*-test. Experiments in **a–e** were performed twice with comparable results.

acidification rate (ECAR):OCR ratio (Fig. 2b), and we observed both an extremely low glycolysis:OXPPOS ratio and restored lactate production following ectopic expression of PGD (Fig. 2a).

Furthermore, IACS-010759 treatment resulted in >70% reduction in viability and a two- to fivefold increase in apoptosis in NB-1, Gli56, or D423 cells, whereas ectopic expression of either ENO1 or

PGD (Fig. 2c,d and Supplementary Fig. 6a–c) substantially attenuated the response. Similarly, the viability of *ENO1*^{-/-} or *ENO1*^{+/-} glioma sphere-derived cell lines was reduced upon IACS-010759 exposure (Supplementary Fig. 6d–f). These data are consistent with our hypothesis that glycolysis deficiency renders cell lines highly sensitive to OXPHOS inhibitors, such as IACS-010759.

AML tumor cells are sensitive to IACS-010759. Previous reports have suggested that leukemia cells are highly dependent on OXPHOS^{6,7,11–13,38–40}, warranting evaluation of IACS-010759 in AML models. Established AML cell lines were exposed to a range of IACS-010759 concentrations for 3–7 d, resulting in reduced viability with half-maximal effective concentration (EC_{50}) values of < 3 nM (Fig. 2e and Supplementary Fig. 7a). Although the inflection point of response (at the EC_{50} point on the dose-response curve) was equivalent across cell lines (Supplementary Fig. 7a), the effect of IACS-010759 on viability varied, with MOLM-13 (in which FLT3 has an internal tandem duplication (ITD) mutation) being relatively insensitive (Fig. 2e). Treatment with IACS-010759 uniformly reduced OCR, indicating that the differential effects on viability are not due to the lack of OXPHOS inhibition. This is consistent with our finding of similar EC_{50} values across cell lines (Supplementary Fig. 7b). In most cell lines, IACS-010759 treatment modestly increased apoptosis by up to twofold (Fig. 2h). Cells responded more robustly to IACS-010759 treatment when glucose availability was restricted, whereas glutamine restriction did not enhance the response (Supplementary Fig. 7c,d), which is consistent with glucose utilization being the primary compensatory response to OXPHOS inhibition. Interestingly, MOLM-13 had the highest baseline OCR and largest glycolytic reserve of the evaluated cell lines, and both of these factors may contribute to its relative insensitivity to IACS-010759 (Supplementary Fig. 7b). This might represent a potential mechanism underlying treatment resistance and is consistent with results reported for OXPHOS inhibition in melanoma models⁴¹. We extended our studies to primary AML blasts isolated from peripheral blood of patients with relapsed/refractory AML by treating blasts *ex vivo* with multiple concentrations of IACS-010759 for up to 5 d. In nearly all primary AML samples, but not in non-transformed mononuclear cells isolated from normal bone marrow, IACS-010759 reduced viability and induced apoptosis (Fig. 2f,g,i,j and Supplementary Table 2), consistent with our observations in AML cell lines and supporting the existence of a therapeutic window in which IACS-010759 can selectively target leukemic versus normal hematopoietic cells. The patient-derived xenograft (PDX-4030094) also responded robustly to IACS-010759 (approximate IC_{50} < 1.5 nM) upon *ex vivo* treatment (Supplementary Fig. 7e). Further, we evaluated IACS-010759 response in cell lines established from two previously described murine AML models genetically engineered to ectopically coexpress the clinically relevant translocation between *KMT2A* (also known as mixed-lineage leukemia, *MLL*) and *MLLT1* (*ENL*) in a *KRAS*^{G12P} background with or without *TP53* deletion⁴². Viability and OCR were equally inhibited in both cell lines (Supplementary Fig. 7f,g) with approximate IC_{50} values of 20 nM and 55 nM, respectively. These results, taken together with those from *ENO1*- and PGD-null GBM models, define two biological tumor contexts with striking sensitivity to IACS-010759.

IACS-010759 safely targets glycolysis-deficient tumors in vivo.

To determine whether the observed *in vitro* and *ex vivo* effects predicted *in vivo* responses in preclinical models at tolerated doses, we evaluated IACS-010759 in mouse models of glioblastoma and/or neuroblastoma and AML. The PK profile of IACS-010759 was determined in mice following intravenous (0.3 mg per kg body weight (mg/kg)) and oral (1 mg/kg) administration (Supplementary Fig. 8a). IACS-010759 was characterized by low plasma clearance with a high volume of distribution, resulting in a prolonged terminal

half-life (>24 h) of IACS-010759 with sustained levels of compound in the plasma following oral dosing. Conversion of IACS-010759 free base into the corresponding HCl salt (IACS-010759.HCl) resulted in a ~10-fold increase in plasmatic exposure after oral dosing (Supplementary Fig. 8b). We did not observe changes in blood glucose level with single or repeated doses of IACS-010759 (Supplementary Fig. 8c), which is consistent with previous reports for metformin⁴³. However, at 2 h after the first or fifth dose, plasma insulin levels transiently decreased and returned to control levels by 24 h postdose (Supplementary Fig. 8d).

To assess the tolerability and antitumor activity of IACS-010759 in a glycolysis-deficient context, mice bearing NB-1 (PGD-null) subcutaneous xenografts received daily oral doses of 0, 5, 10, or 25 mg/kg IACS-010759 free base per day for 21 d. Treatment with IACS-010759 at the 5 or 10 mg/kg dose resulted in tumor regression with minimal body weight loss (Fig. 3a and Supplementary Fig. 8e), whereas IACS-010759 at the 25 mg/kg dose was not tolerated, and body weight loss (Supplementary Fig. 8e), lethargy and hypothermia were observed. At the tolerated doses, IACS-010759 was equally effective and well tolerated when administered in various intermittent dosing schedules (Supplementary Fig. 8f,g), providing flexibility for dosing. Transient, intermittent treatment of Gli56 intracranial tumors with 5 mg/kg IACS-010759.HCl using a 5 d on and 2 d off (5 on/2 off) schedule for 4 weeks reduced tumor size as measured through magnetic resonance imaging (MRI) (Fig. 3b,c) and extended median survival from 84 d to 130 d (Supplementary Fig. 9a). Tumor hypoxia was eliminated in Gli56 and D423 intracranial tumors after two daily doses of 5 mg/kg IACS-010759.HCl (Supplementary Fig. 9b,c), whereas tumor hypoxia persisted in vehicle-treated control animals, supporting the occurrence of OXPHOS inhibition within the tumor. We also observed reductions of 84% and 43% in the number of cells positive for the mitotic marker phosphorylated histone H3 in IACS-010759.HCl-treated Gli56 and D423 tumors, respectively, compared to control animals (Supplementary Fig. 9d–g), which is indicative of reduced tumor cell proliferation in the inhibitor-treated animals. Collectively these data provide evidence of profound antitumor activity of IACS-010759 at well-tolerated doses in the context of glycolysis-deficient brain tumors.

Immunohistochemistry (IHC) analysis of tumor samples from 92 patients treated at The University of Texas MD Anderson Cancer Center was conducted to determine the prevalence of *ENO1*- and PGD-null GBM with the aim of defining a potential path for clinical treatment. Eight tumors (8.6%) were either unambiguously *ENO1*-null (3.3%) or showed very low *ENO1* staining (five tumors (5.3%)), which represented a slightly higher percentage of *ENO1*-null tumors compared to reports from The Cancer Genome Atlas (TCGA) sequencing data (Fig. 3d and Supplementary Fig. 9h). Whether tumors with weak staining represent a nonspecific background or very low expression of *ENO1* could not be ascertained and will require independent validation with orthogonal assays. Regardless, a clinically relevant population with at least 3.3% of GBM tumors being *ENO1*-null was clearly identified. It should be noted that the strong, residual signal represents *ENO1* expression in nontumor stromal cells, such as microglia, lymphoid cells, and blood vessel endothelial and smooth muscle cells (Supplementary Figs. 9i,j and 10a–d). No PGD-null tumors were identified. On the basis of this analysis, we conclude that *ENO1*-null GBM tumors can be detected and therefore represent a viable, clinically relevant population expected to benefit from treatment with IACS-010759.

IACS-010759 is tolerated and extends survival in mouse models of AML. *In vivo* AML models were evaluated to confirm the antitumor activity and tolerability of IACS-010759 in this context. The OCI-AML3 cell line, PDX-4030094 (*MLL*-rearranged AML PDX model refractory to standard-of-care treatment),

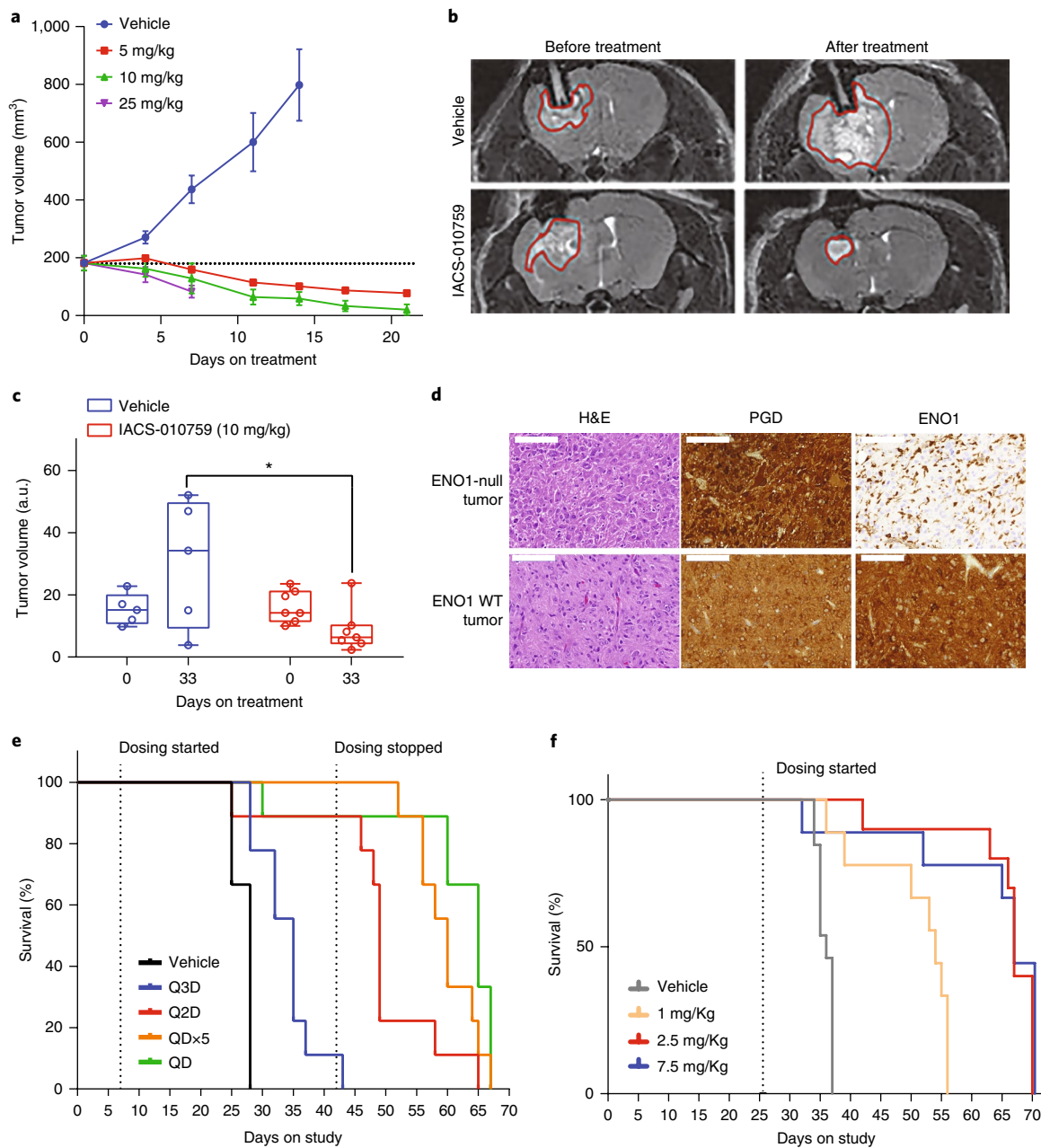


Fig. 3 | Glycolysis-deficient and AML xenografts are sensitive to OXPHOS inhibition. a, Tumor volume of subcutaneous NB1 tumors in mice that received daily oral dosing of IACS-010759 or vehicle ($n=10$ per group; data represents mean \pm s.e.m.). **b,c**, Mice that received intracranial implantation of ENO1-null Gli56 cells were treated with vehicle or 5 mg/kg IACS-010759 for 4 weeks following a 5 on/2 off dosing schedule. Representative pre- and post-treatment magnetic resonance imaging (MRI) coronal images of brain (vehicle, $n=5$ mice; IACS-010759, $n=7$ mice; experiment repeated once with similar results) (**b**) and quantitation of tumor volumes calculated from MRI images at Day 33 (**c**) are shown. For box plots, midlines indicate the median, upper and lower perimeters indicate first and third quartiles, and tails indicate the minimum and maximum. Each point is an independent mouse. $*P=0.025$ by two-sided Student's t -test. a.u., arbitrary units. **d**, H&E and immunohistochemistry staining for 6PGD and ENO1 protein expression in an array of tumors from patients with GBM. Representative images from wild-type ENO1 (ENO1 WT; $n=84$) and ENO1-null ($n=8$) tumors are shown. Scale bars, 100 μ m. **e**, Kaplan-Meier survival analysis of mice inoculated with OCI-AML3 cells and treated for 5 weeks (starting on Day 7) with oral vehicle or with 10 mg/kg IACS-010759 daily (QD), 5 on/2 off (QDx5), every other day (Q2D), or every third day (Q3D) ($n=9$ mice per group). $P=0.0007$ (Q3D), 0.0008 (Q2D), and <0.0001 (QD and QDx5) by Mantel-Cox log-rank test. **f**, Kaplan-Meier survival analysis of mice inoculated with primary patient sample 4030094 and orally treated with 1, 2.5, or 7.5 mg/kg IACS-010759 daily starting on Day 25 ($n=9$ mice per group). $P=0.0002$ (1 mg/kg) and $P<0.0001$ (2.5 and 7.5 mg/kg) by Mantel-Cox log-rank test.

PDX-S6-AP (PDX with complex cytogenetics and unfavorable prognosis) and three genetically defined murine leukemia syngeneic models⁴² were grown orthotopically in mice. Seven days after inoculation with OCI-AML3 cells, mice were orally dosed

for 35 d with 10 mg/kg IACS-010759.HCl or vehicle using several intermittent schedules (Fig. 3e) and doses that were all well tolerated (Supplementary Fig. 11a,c). Daily dosing schedules, QD (daily) or QDx5 (5 d on/2 d off), were most effective and

increased median survival from 28 d to longer than 60 d, whereas less-frequent dosing schedules (Q2D or Q3D) enhanced survival to a lesser extent (Fig. 3e). In the PDX-4030094 model, 2.5 or 7.5 mg/kg IACS-010759.HCl per day nearly doubled median survival from 35 d to almost 70 d (Fig. 3f and Supplementary Fig. 11b), whereas 1 mg/kg IACS-010759.HCl per day extended survival to 55 d. Additionally, disease burden, as measured by splenic hCD45 abundance at treatment day 21, was significantly reduced in IACS-010759-treated groups relative to vehicle-treated groups (Supplementary Fig. 11d). IACS-10759 similarly improved survival in the PDX-S6-AP model (Supplementary Fig. 11e). Treatment of the highly aggressive, matched-pair *MLL-ENL* translocation syngeneic models with IACS-010759 resulted in modest but statistically significant prolonged survival in the *TP53*^{-/-} model, but not the *TP53*^{+/+} model (Supplementary Fig. 11f,g). In contrast, the mouse syngeneic model, AML1/ETO9a (KRAS-G12D, p53-null), was more sensitive to IACS-010759. In this model, there were significant decreases in disease burden at days 8 (42%) and 15 (24%) following treatment (Supplementary Fig. 11h), and median survival was statistically significantly extended from 17 d to 21 d (24%) (Supplementary Fig. 11i). Similarly to the xenograft models, all three syngeneic models experienced transient loss of body weight during the first week of dosing (Supplementary Fig. 11j-l). Overall, the consistent anti-leukemic responses observed in vitro and in vivo provided the preclinical rationale to evaluate IACS-010759 in a phase 1 study in subjects with relapsed/refractory AML (NCT02882321), which enrolled its first subject in October 2016.

OXPPOS inhibition leads to depletion of energy and nucleotide biosynthesis. To better understand the molecular mechanism through which IACS-010759 exerts antitumor activity, we performed metabolomic analyses, stable-isotope tracing experiments, and functional characterization on a subset of AML cell lines. IACS-010759 induced modest increases in reactive oxygen species (ROS) levels, consistent with previous reports examining OXPPOS inhibition^{41,44} (Supplementary Fig. 12a). To evaluate metabolic reprogramming, OCI-AML3 cells were exposed to IACS-010759 for 6, 24, or 72 h, and the resultant cell lysates were subjected to liquid chromatography–mass spectrometry (LC–MS) analysis to measure metabolites from central carbon metabolism and amino acids. IACS-010759 treatment elevated the intracellular steady-state level of the complex I substrate, NADH, as well as that of nucleotide monophosphates (NMPs), whereas it reduced levels of nucleotide triphosphates (NTPs); all of these changes are consistent with complex I inhibition and reduced energetic status (Fig. 4a). This was further confirmed by elevated pT172-AMPK levels (Fig. 4j and Supplementary Fig. 12m), a well-established readout of energetic stress. Stable isotope–tracing experiments using uniformly labeled [¹³C]glucose (Fig. 4b) revealed that IACS-010759 significantly increased incorporation of [¹³C]glucose into the glycolysis endpoints lactate and alanine, as evaluated by M+3 isotopologue fractions (Fig. 4c), and decreased incorporation into the tricarboxylic acid (TCA) cycle intermediates and mitochondria-produced metabolites (M+2 isotopologue fractions), including aspartate and glutamate (Fig. 4d), suggesting that glucose utilization through these pathways was substantially reduced. Although IACS-010759-treated cells uptake less glutamine than control cells do (Supplementary Fig. 12b), tracing experiments with uniformly labeled [¹³C]glutamine confirmed that treatment with IACS-010759 increased incorporation of [¹³C]glutamine carbons into the TCA cycle to fuel both oxidative and reductive metabolism, likely to support fatty acid biosynthesis, but failed to productively contribute toward aspartate synthesis (Supplementary Fig. 12c–f)⁴⁵. These observations suggest an increased utilization of glutamine as an alternative compensatory mechanism to IACS-010759 treatment.

Targeted metabolomics in OCI-AML3 cells showed that, among all amino acids measured, aspartate was the only other amino acid reduced by IACS-010759 (Fig. 4e), which is consistent with other published findings^{16,17}. To assess whether aspartate was incorporated into nucleotides, as has been suggested^{16,17}, OCI-AML3 cells were grown with uniformly labeled [¹³C]aspartate. After treatment with IACS-010759, an increased M+3 isotopologue fraction of several nucleotides was observed (Fig. 4f,g) that was consistent with increased utilization of exogenous aspartate for nucleotide biosynthesis, which suggests that mitochondria-produced aspartate becomes rate limiting upon OXPPOS inhibition. Although aspartate supplementation partially restored cell growth (Fig. 4h and Supplementary Fig. 12g,h), cell cycle progression, and incorporation of BrdU into cycling cells (Fig. 4i and Supplementary Fig. 12i), it failed to influence pT172-AMPK activation, indicating persistent energetic stress (Fig. 4j and Supplementary Fig. 12m). Interestingly, AMPK activation does not appear to be essential for the reduced tumor cell viability observed upon IACS-010759 exposure, as shRNA-mediated knockdown of AMPK in OCI-AML3 cells minimally impacted cell viability (Supplementary Fig. 12j,k). Aspartate also abrogated IACS-010759-induced accumulation of DNA damage, as measured by p^{S139}-γH2AX levels (Fig. 4j). Interestingly, aspartate supplementation was not able to rescue the proliferation phenotype in the relatively insensitive MOLM-13 cell line, suggesting that the hypersensitive cell lines may rely on OXPPOS for energy as well as aspartate production (Supplementary Fig. 12h). As an additional response mechanism, we found that IACS-010759 markedly increased expression of the CD14 myeloid differentiation marker in OCI-AML3 cells (Supplementary Fig. 12l), but not in MOLM-13 cells (data not shown). Taking these data together, we propose that the IACS-010759-mediated reduction in cell viability and induction of differentiation or apoptosis result from a combination of energy depletion and reduced aspartate production (Fig. 5a,b).

Therapeutic targeting of OXPPOS in AML. On the basis of mechanisms defined in vitro studies, we evaluated the effects of IACS-010759 on OCR, aspartate, proliferation, and differentiation status in blast cells from PDX-4030094 in vivo. Blast cells were harvested from mouse spleens 2 h after the first dose or 24 h after a second dose of IACS-010759.HCl (representing C_{max} and C_{min}, respectively; Fig. 5b). At each dose and time point, OCR, aspartate, and an IACS-010759-regulated transcriptomic signature (Supplementary Fig. 13a–f) were measured to establish a relationship among PK, pharmacodynamic (PD), and efficacy outcomes. At 2 h, OCR was equally inhibited at all doses (Fig. 5c and Supplementary Fig. 14a). By 48 h, OCR (Fig. 5d and Supplementary Fig. 14b), aspartate (Fig. 5f), and the gene expression signature (Fig. 5g) were suppressed in a dose-dependent manner at both 2.5- and 7.5-mg doses of IACS-010759, and these measures correlated with increased survival (see Fig. 3f). At both time points, aspartate levels were unaltered at a dose of 1 mg/kg IACS-010759 but were suppressed in a dose-dependent manner at the top two doses (Fig. 5e,f), suggesting that aspartate level is a less-sensitive measure than OCR or the gene expression signature. Blasts isolated from mice that received two doses of IACS-010759 (7.5 mg/kg) exhibited reduced proliferation (Fig. 5h) and increased apoptosis (Fig. 5i). Additionally, IACS-010759 treatment reduced the fraction of CD34⁺ stem and progenitor AML cells (Fig. 5j) in a dose-dependent manner, most likely owing to induction of leukemia cell differentiation, as suggested by enrichment of AML cells expressing the myeloid differentiation antigens myeloid cell nuclear differentiation antigen (MND1), CD14, CD11b, and CD68 (Fig. 5k and Supplementary Fig. 15a–k). These data support employing OCR, aspartate levels, gene expression changes, and markers of differentiation as PD biomarkers to assess the biology of response in clinical samples from patients with relapsed/refractory AML treated with OXPPOS inhibitors, such as IACS-010759.

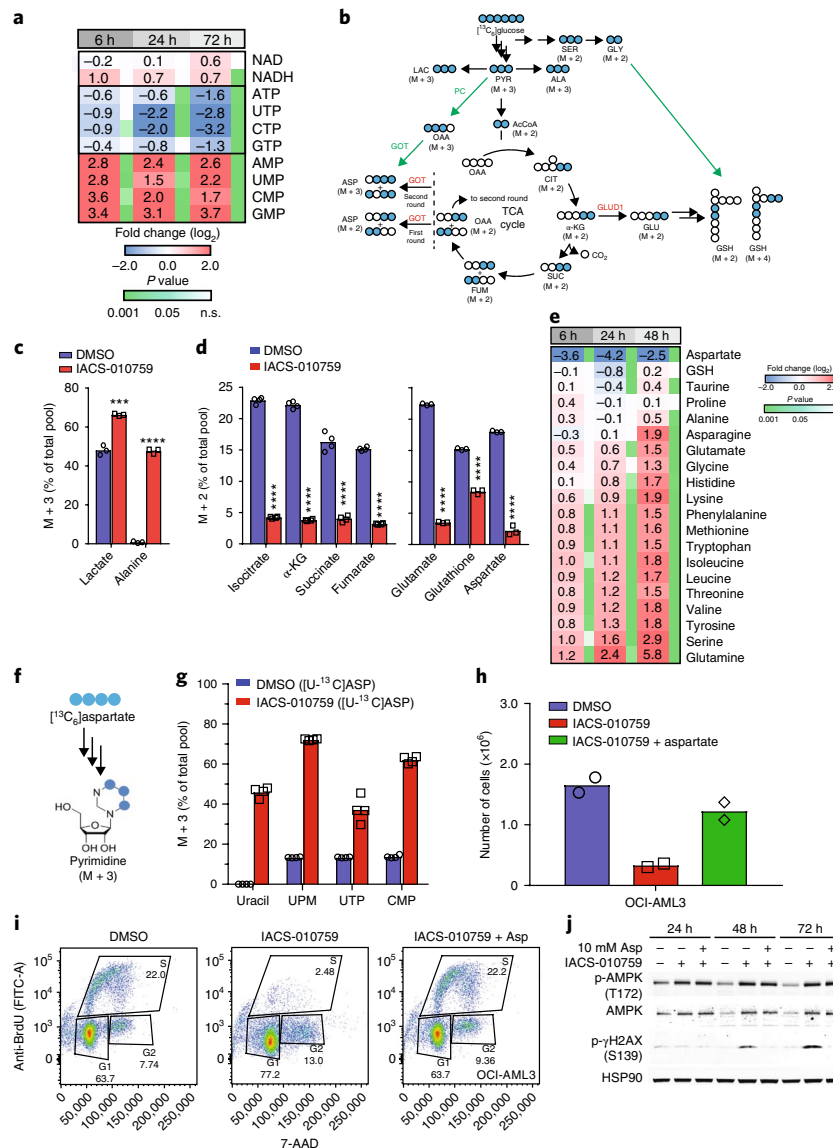


Fig. 4 | Inhibition of OXPHOS by IACS-010759 leads to energy deprivation and impairs nucleotide biosynthesis. a, Targeted metabolomic analysis of nucleotide biomolecules in OCI-AML3 cells treated with 100 nM IACS-010759 for 6, 24, or 72 h. The heat map depicts alterations of metabolites associated with complex I and energy production as fold change (\log_2) of IACS-010759-treated cells versus DMSO-treated controls ($n = 4$ cultures; the experiment was repeated once with comparable results). Data are shown as mean values. P values were derived by two-sided Welch's t -test accounting for unequal variance; n.s., nonsignificant. **b**, Illustration of [^{13}C]glucose metabolism in OCI-AML3 cells. White circles, ^{12}C carbons; blue circles, ^{13}C carbons. M + 2 and M + 3 refer to the number of ^{13}C carbons. **c**, Cells were grown in culture medium containing [^{13}C]glucose and were treated with DMSO or 100 nM IACS-010759 for 24 h. Incorporation of [^{13}C]glucose into glycolysis endpoints (lactate (extracellular) and alanine (intracellular)) is shown. Data are plotted as mean values and individual data points from $n = 4$ cultures. *** $P = 0.0002$, **** $P < 0.0001$ by two-sided Student's t -test. **d**, TCA intermediates (isocitrate, α -ketoglutarate (α -KG), succinate, and fumarate (intracellular)) and mitochondria metabolites (glutamate, glutathione, and aspartate (intracellular)) in OCI-AML3 cells after treatment with DMSO or 100 nM IACS-010759 for 24 h. Data are plotted as mean values and individual data points from $n = 4$ cultures; the experiment was performed twice with comparable results. **** $P < 0.0001$ by two-sided Student's t -test. **e**, Targeted metabolomic analysis of amino acid biomolecules in OCI-AML3 cells treated with DMSO or 100 nM IACS-010759 for 6, 24, or 72 h. The heat map depicts alterations of metabolite levels noted as fold-change (\log_2) of IACS-010759-treated cells versus DMSO-treated controls. P values were derived using two-sided Welch's t -test accounting for unequal variance. Data are plotted as mean values and individual data points from $n = 4$ cultures; the experiment was repeated once with comparable results. **f**, Illustration of the conversion of [^{13}C]aspartate carbon into pyrimidines. Blue circles depict carbons derived from aspartate. **g**, Incorporation of carbons derived from [^{13}C]aspartate ([^{13}C]ASP) into representative pyrimidine metabolites in OCI-AML3 cells treated with DMSO or 100 nM IACS-010759 for 72 h. Data are plotted as mean values and individual data points from $n = 4$ cultures; the experiment was performed twice with comparable results. **h**, OCI-AML3 cells were cultured in medium treated with DMSO, 100 nM IACS-010759, or 100 nM IACS-010759 supplemented with 10 mM aspartate, and the number of cells was measured after 72 h. Data are plotted as mean values and individual data points from $n = 2$ cultures; the experiment was performed twice with comparable results. **i**, Incorporation of BrdU into DNA was measured through flow cytometry, in OCI-AML3 cells treated for 72 h with DMSO, 123 nM IACS-010759, or 123 nM IACS-010759 supplemented with 10 mM aspartate. Cells were also stained with 7-AAD to detect DNA. **j**, Immunoblot for activated AMPK (phosphorylated AMPL (p-AMPK), T172) and γ -H2AX (p- γ -H2AX, S139) in OCI-AML3 cells that were treated as described in the Methods. See Supplementary Fig. 12m for blots with molecular weight markers. Experiments in **i** and **j** were repeated once with comparable results.

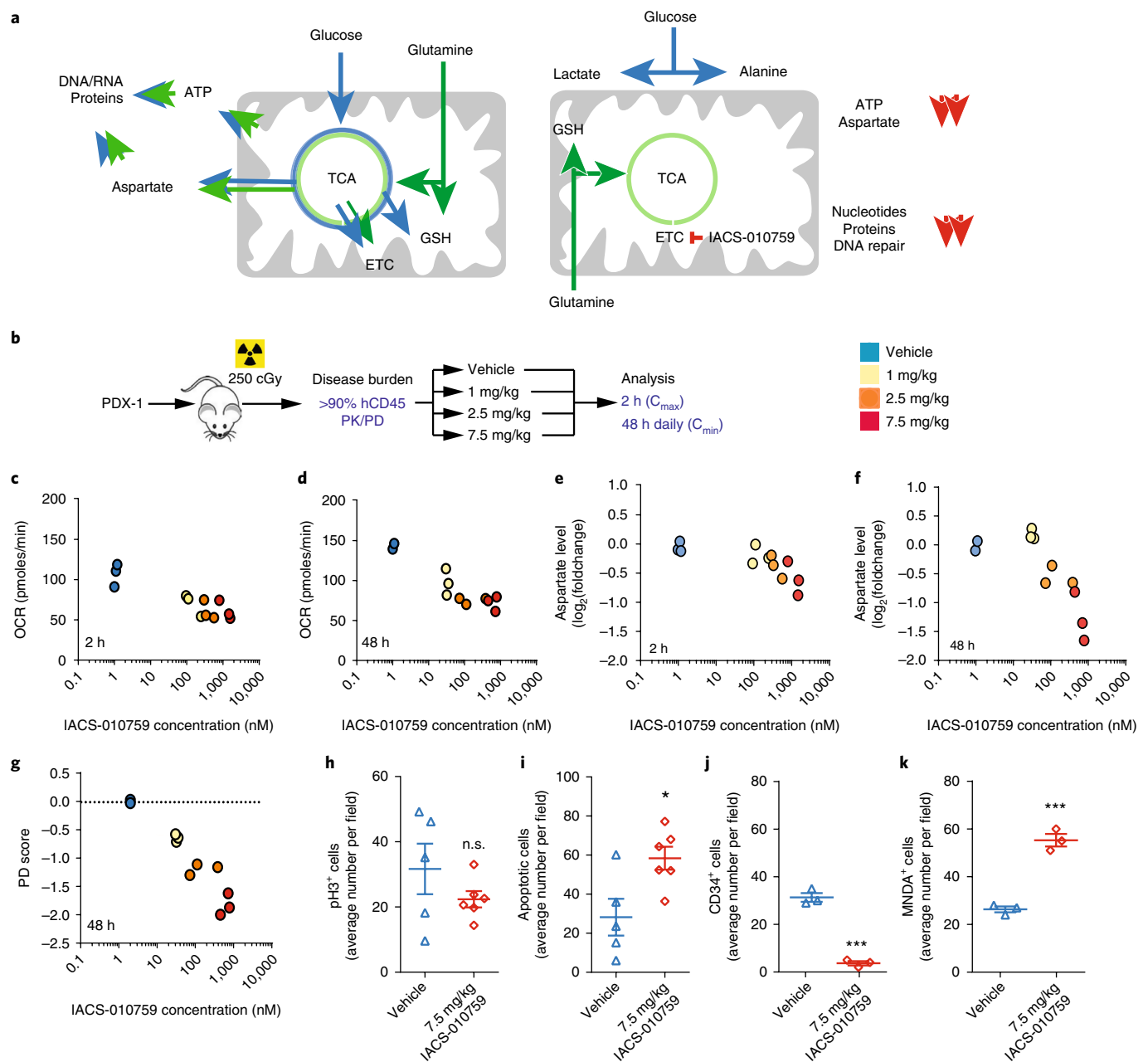


Fig. 5 | IACS-010759 modulates several clinically translatable pharmacodynamic biomarkers. a, Model showing glucose and glutamine utilization by the TCA cycle to produce ATP and aspartate, which are used for nucleotide biosynthesis (left), and the changes that occur when complex I is inhibited by IACS-010759 (right). **b**, Schematic of workflow for assessment of PD markers of target inhibition and biology of response. After irradiation and inoculation, tumor burden was monitored. Upon reaching 90% tumor burden in the spleen (high human CD45⁺ cells compared to mouse CD45⁺ cells), mice received two doses of IACS-010759 that were administered 24 h apart. Tumor cells were isolated from the spleen at 2 h after the first dose or at 24 h after the second dose (2-h (C_{max}) and 48-h (C_{min}) time points, respectively). **c,d**, OCR of leukemia cells normalized to the cell number at the 2-h (**c**) and 48-h (**d**) time points. **e,f**, Aspartate levels of leukemia cells at the 2-h (FC = fold-change) (**e**) and 48-h (**f**) time points. **g**, Change in expression of a 19-gene (pharmacodynamic (PD)) score for leukemia cells at the 48-h time point. **h-k**, Average number of phosphorylated Histone H3 (p-H3)⁺ cells (**h**), apoptotic cells measured by cleaved caspase 3 (**i**), CD34⁺ cells (**j**), or MNDA⁺ cells (**k**) per field in the spleens of mice treated with vehicle or IACS-010759 at the 48-h time point. In **c-g**, each symbol represents the mean value for three technical replicates from a single mouse. In **h-k**, each symbol represents the mean of five random fields from a single mouse, and the overall mean \pm s.e.m. is shown. * $P = 0.02$, *** $P < 0.001$ by two-sided Student's *t*-test.

Advancing IACS-010759 into clinical evaluation. The antitumor activity of IACS-010759 in glycolysis-deficient GBM and/or neuroblastoma tumors and relapsed/refractory AML justified evaluation of IACS-010759 in clinical studies. During preclinical development, we evaluated IACS-010759 PK in mouse, rat, dog, and cynomolgus monkey; these PK profiles indicated that the compound displayed low clearance, large volume of distribution, and long terminal half-life

(Supplementary Table 3). In a battery of in vitro studies, IACS-010759 did not show any concerning effects in binding assays on a panel of 80 receptors and ion channels (Supplementary Table 4), nor did IACS-010759 inhibit the human ERG K⁺ channel current ($IC_{50} > 30 \mu M$) (Supplementary Fig. 16) or modulate CYP enzyme activity (data not shown). In in vivo toxicity studies, including dose-range finding, acute intravenous dosing, repeated oral dosing

(both daily and intermittent), and a pivotal good laboratory practice (GLP)-compliant 28-d oral toxicity study with a 28-d recovery period in the Sprague–Dawley rat and cynomolgus monkey, drug-related adverse events included emesis and decreased body weight at lower doses. At the highest doses, decreased core body temperature and death were observed, which are consistent with anticipated effects of excessive OXPHOS inhibition. No-observed-adverse-effect dose levels (NOAELs) were identified in rat and monkey that supported the ability for oral daily doses to yield plasma drug concentrations above the anticipated amount needed to result in on-target drug effects. These data were used to establish the human starting dose per Food and Drug Administration (FDA) guidelines⁴⁶.

Discussion

Our findings contrast with the century-old tenet, put forth in Otto Warburg's seminal work, that glycolysis is the dominant metabolic pathway to which tumors become addicted¹. In recent years, the field has dispelled the notion that the increased glycolysis observed in tumors is simply a mechanism for providing additional energy to support the high rate of proliferation, and instead has indicated that the adaptation serves to provide macromolecule building blocks for biosynthetic processes that are critical for enhanced tumor growth. Through the development and characterization of IACS-010759, we now provide evidence that clinically translatable contexts exist in which tumors are highly dependent on OXPHOS for survival. We further demonstrate that subsets of tumors depend on OXPHOS not only for ATP synthesis, but also to produce the macromolecules necessary for biosynthetic processes, similar to glycolysis. In the most sensitive tumor cells, OXPHOS disruption creates an environment of energy and macromolecule depletion that leads to cell cycle arrest, apoptosis, and, in the case of AML, differentiation, similar to what has been reported with small-molecule inhibitors of mutant IDH⁴⁷. Taken together, our preclinical data support clinical evaluation of IACS-010759 in AML and solid tumors that lack compensatory glycolytic capacity. First-in-human clinical studies with IACS-010759 are ongoing in patients with AML and solid tumors to establish proof of concept, define the maximum tolerated dose, and provide initial verification of the hypotheses generated by this work.

Methods

Methods, including statements of data availability and any associated accession codes and references, are available at <https://doi.org/10.1038/s41591-018-0052-4>.

Received: 11 January 2018; Accepted: 27 March 2018;

Published online: 11 June 2018

References

- Warburg, O., Wind, F. & Negelein, E. The metabolism of tumors in the body. *J. Gen. Physiol.* **8**, 519–530 (1927).
- Palaskas, N. et al. ¹⁸F-fluorodeoxy-glucose positron emission tomography marks MYC-overexpressing human basal-like breast cancers. *Cancer Res.* **71**, 5164–5174 (2011).
- DeBerardinis, R. J. & Chandel, N. S. Fundamentals of cancer metabolism. *Sci. Adv.* **2**, e1600200 (2016).
- Koppenol, W. H., Bounds, P. L. & Dang, C. V. Otto Warburg's contributions to current concepts of cancer metabolism. *Nat. Rev. Cancer* **11**, 325–337 (2011).
- Caro, P. et al. Metabolic signatures uncover distinct targets in molecular subsets of diffuse large B cell lymphoma. *Cancer Cell* **22**, 547–560 (2012).
- Goto, M. et al. Importance of glutamine metabolism in leukemia cells by energy production through TCA cycle and by redox homeostasis. *Cancer Invest.* **32**, 241–247 (2014).
- Goto, M. et al. Adaptation of leukemia cells to hypoxic condition through switching the energy metabolism or avoiding the oxidative stress. *BMC Cancer* **14**, 76 (2014).
- Haq, R. et al. Oncogenic BRAF regulates oxidative metabolism via PGC1 α and MITF. *Cancer Cell* **23**, 302–315 (2013).
- Hu, J. et al. Heterogeneity of tumor-induced gene expression changes in the human metabolic network. *Nat. Biotechnol.* **31**, 522–529 (2013).
- Roesch, A. et al. Overcoming intrinsic multidrug resistance in melanoma by blocking the mitochondrial respiratory chain of slow-cycling JARID1B^{high} cells. *Cancer Cell* **23**, 811–825 (2013).
- Simsek, T. et al. The distinct metabolic profile of hematopoietic stem cells reflects their location in a hypoxic niche. *Cell Stem Cell* **7**, 380–390 (2010).
- Skrtić, M. et al. Inhibition of mitochondrial translation as a therapeutic strategy for human acute myeloid leukemia. *Cancer Cell* **20**, 674–688 (2011).
- Sriskanthadevan, S. et al. AML cells have low spare reserve capacity in their respiratory chain that renders them susceptible to oxidative metabolic stress. *Blood* **125**, 2120–2130 (2015).
- Vazquez, F. et al. PGC1 α expression defines a subset of human melanoma tumors with increased mitochondrial capacity and resistance to oxidative stress. *Cancer Cell* **23**, 287–301 (2013).
- Viale, A. et al. Oncogene ablation-resistant pancreatic cancer cells depend on mitochondrial function. *Nature* **514**, 628–632 (2014).
- Birsoy, K. et al. An essential role of the mitochondrial electron transport chain in cell proliferation is to enable aspartate synthesis. *Cell* **162**, 540–551 (2015).
- Sullivan, L. B. et al. Supporting aspartate biosynthesis is an essential function of respiration in proliferating cells. *Cell* **162**, 552–563 (2015).
- Bridges, H. R., Jones, A. J., Pollak, M. N. & Hirst, J. Effects of metformin and other biguanides on oxidative phosphorylation in mitochondria. *Biochem. J.* **462**, 475–487 (2014).
- Dykens, J. A. et al. Biguanide-induced mitochondrial dysfunction yields increased lactate production and cytotoxicity of aerobically-poised HepG2 cells and human hepatocytes in vitro. *Toxicol. Appl. Pharmacol.* **233**, 203–210 (2008).
- Wang, D. S. et al. Involvement of organic cation transporter 1 in hepatic and intestinal distribution of metformin. *J. Pharmacol. Exp. Ther.* **302**, 510–515 (2002).
- Sanchez, M., Gastaldi, L., Remedi, M., Cáceres, A. & Landa, C. Rotenone-induced toxicity is mediated by Rho-GTPases in hippocampal neurons. *Toxicol. Sci.* **104**, 352–361 (2008).
- Ellinghaus, P. et al. BAY 87-2243, a highly potent and selective inhibitor of hypoxia-induced gene activation has antitumor activities by inhibition of mitochondrial complex I. *Cancer Med.* **2**, 611–624 (2013).
- Li, S. H. et al. A novel mode of action of YC-1 in HIF inhibition: stimulation of FIH-dependent p300 dissociation from HIF-1 α . *Mol. Cancer Ther.* **7**, 3729–3738 (2008).
- Lin, X. et al. A chemical genomics screen highlights the essential role of mitochondria in HIF-1 regulation. *Proc. Natl. Acad. Sci. USA* **105**, 174–179 (2008).
- Bai, Y. et al. Lack of complex I activity in human cells carrying a mutation in MtDNA-encoded ND4 subunit is corrected by the *Saccharomyces cerevisiae* NADH-quinone oxidoreductase (NDI1) gene. *J. Biol. Chem.* **276**, 38808–38813 (2001).
- Seo, B. B. et al. Molecular remedy of complex I defects: rotenone-insensitive internal NADH-quinone oxidoreductase of *Saccharomyces cerevisiae* mitochondria restores the NADH oxidase activity of complex I-deficient mammalian cells. *Proc. Natl. Acad. Sci. USA* **95**, 9167–9171 (1998).
- Petrova-Benedict, R., Buncic, J. R., Wallace, D. C. & Robinson, B. H. Selective killing of cells with oxidative defects in galactose medium: a screening test for affected patient fibroblasts. *J. Inher. Metab. Dis.* **15**, 943–944 (1992).
- Robinson, B. H., Petrova-Benedict, R., Buncic, J. R. & Wallace, D. C. Nonviability of cells with oxidative defects in galactose medium: a screening test for affected patient fibroblasts. *Biochem. Med. Metab. Biol.* **48**, 122–126 (1992).
- Zhu, J., Vinothkumar, K. R. & Hirst, J. Structure of mammalian respiratory complex I. *Nature* **536**, 354–358 (2016).
- Chang, E. et al. ¹⁸F-FAZA PET imaging response tracks the reoxygenation of tumors in mice upon treatment with the mitochondrial complex I inhibitor BAY 87-2243. *Clin. Cancer Res.* **21**, 335–346 (2015).
- Krebs, H. A. The Pasteur effect and the relations between respiration and fermentation. *Essays Biochem.* **8**, 1–34 (1972).
- Hao, W., Chang, C. P., Tsao, C. C. & Xu, J. Oligomycin-induced bioenergetic adaptation in cancer cells with heterogeneous bioenergetic organization. *J. Biol. Chem.* **285**, 12647–12654 (2010).
- Leonard, P. G. et al. SF2312 is a natural phosphonate inhibitor of enolase. *Nat. Chem. Biol.* **12**, 1053–1058 (2016).
- Muller, F. L. et al. Passenger deletions generate therapeutic vulnerabilities in cancer. *Nature* **488**, 337–342 (2012).
- Gaitonde, M. K., Murray, E. & Cunningham, V. J. Effect of 6-phosphogluconate on phosphoglucose isomerase in rat brain in vitro and in vivo. *J. Neurochem.* **52**, 1348–1352 (1989).
- Jeffery, C. J., Hardré, R. & Salmon, L. Crystal structure of rabbit phosphoglucose isomerase complexed with 5-phospho-d-arabinonate identifies the role of Glu357 in catalysis. *Biochemistry* **40**, 1560–1566 (2001).

37. Sukhatme, V. P. & Chan, B. Glycolytic cancer cells lacking 6-phosphogluconate dehydrogenase metabolize glucose to induce senescence. *FEBS Lett.* **586**, 2389–2395 (2012).
38. Boultonwood, J. et al. Amplification of mitochondrial DNA in acute myeloid leukaemia. *Br. J. Haematol.* **95**, 426–431 (1996).
39. Lagadinou, E. D. et al. BCL-2 inhibition targets oxidative phosphorylation and selectively eradicates quiescent human leukemia stem cells. *Cell Stem Cell* **12**, 329–341 (2013).
40. Samudio, I. et al. Pharmacologic inhibition of fatty acid oxidation sensitizes human leukemia cells to apoptosis induction. *J. Clin. Invest.* **120**, 142–156 (2010).
41. Schöckel, L. et al. Targeting mitochondrial complex I using BAY 87-2243 reduces melanoma tumor growth. *Cancer Metab.* **3**, 11 (2015).
42. Zuber, J. et al. Mouse models of human AML accurately predict chemotherapy response. *Genes Dev.* **23**, 877–889 (2009).
43. Wheaton, W. W. et al. Metformin inhibits mitochondrial complex I of cancer cells to reduce tumorigenesis. *eLife* **3**, e02242 (2014).
44. Sancho, P. et al. MYC/PGC-1 α balance determines the metabolic phenotype and plasticity of pancreatic cancer stem cells. *Cell Metab.* **22**, 590–605 (2015).
45. Griss, T. et al. Metformin antagonizes cancer cell proliferation by suppressing mitochondrial-dependent biosynthesis. *PLoS Biol.* **13**, e1002309 (2015).
46. Guidance for Industry on Estimating the Maximum Safe Starting Dose in Initial Clinical Trials for Therapeutics in Adult Healthy Volunteers (Food and Drug Administration, Rockville, MD, USA, 2005).
47. Kernytzky, A. et al. IDH2 mutation-induced histone and DNA hypermethylation is progressively reversed by small-molecule inhibition. *Blood* **125**, 296–303 (2015).

Acknowledgements

We thank members of the Center for Co-Clinical Trials, Institute for Applied Cancer Science, the Glioblastoma (GBM) and AML/MDS Moon Shots for intellectual and financial support. We would especially like to express our gratitude and appreciation to C. Vellano for his help editing and assembling this manuscript; F. F. Lang and J. Gumin for providing GSC models; C. Kingsley and the MDACC Small Animals Imaging Facility; and N. Satani and E. Lin for validation of antibodies and preparation of samples for analysis, D. Bigner for D423 cells and D. N. Louis for Gli56 cells. P.Mo. was supported by The Agilent Technologies Thought Leader Award. R.A.D., A.-N.A.A., R.S., and J.Hi. were supported by The Medical Research Council (MC_U105663141 and MC_UU_00015/2 to J.Hi.). M.K., S.T., A.L., P.Ma., H.M., and Q.Z. were supported by CPRIT grant

RP140218. F.L.M. was supported by the CPRIT RP140612 and National Institutes of Health (NIH) Brain SPORE P50CA127001, and A.C.S. was supported by the Research Scholar Grant RSG1514501CDD. G.F.D. was supported by the American Association for Cancer Research (AACR) 14-90-25 and by the Sheikh Ahmed Bin Zayed Al Nahyan Center for Pancreatic Cancer Grant. This work was supported in part by the Leukemia & Lymphoma Society through its Therapy Acceleration Program (TAP) and by the MD Anderson Moon Shots program.

Author contributions

The studies were designed with input from J.R.Ma., J.R.Mo., Y.S., M.Pr., M.B., J.Ha., C.B., P.Mo., J.Hi., M.K., P.J., M.E.D.F., C.T., T.P.H., G.F.D., and F.M. In vitro experiments were performed by J.R.Ma., J.R.Mo., V.G., L.Ha., Y.T., Y.S., M.Pr., S.G., M.M., T.K., M.B., P.Mo., J.B., G.G., M.G.D., J.Ha., Y.J., T.L., H.M., P.Ma., M.Pe., R.S., T.S., M.S., V.K.H., C.C.C., and Q.Z. IACS-010759 was developed and conceived by M.E.D.F., T.M., C.C., B.C., G.L., Z.K., A.P., J.T., and P.J. In vivo studies were performed by Y.-H. L., N.F., J.Ga., J.Gr., and R.M. Immunohistochemistry was performed by J. Ac., E.C., S.K., and J.R.-C. Computational chemistry was performed by J.Hi. and J.B.C. Pharmacokinetic analysis was performed by S.H., Q.X., and Y.J. FACS data analysis was performed by J.R.Mo. and S.G. Glioma stem cell work was performed by Y.S., T.S., J.-W.D., V.K.H., J.F.d.G., and C.C.C. Bioinformatic analysis was performed by C.B. Clinical positioning in AML was designed by M.K., N.D., J.R.Ma., M.E.D., and P.J. Metabolomic data for glycolysis deficient was generated by Y.S., C.B., and J.As. and for leukemia by J.R.Mo., S.T., A.L., and P.Mo. Stable-isotope labeling study design, analysis and interpretation was performed by P. Mo. Mouse complex I assays were designed and performed by J.Hi., A.-N.A.A., and R.S. Normal bone marrow samples were provided by S.C. and G.A.-A. Writing and preparation of the manuscript and figures were performed by J.R.Ma., J.R.Mo., T.P.H., R.A.D., A.D., Y.S., M.E.D.F., M.K., P. Mo., and P.J.

Competing interests

The authors declare no competing interests.

Additional information

Supplementary information is available for this paper at <https://doi.org/10.1038/s41591-018-0052-4>.

Reprints and permissions information is available at www.nature.com/reprints.

Correspondence and requests for materials should be addressed to J.R.M.

Publisher's note: Springer Nature remains neutral with regard to jurisdictional claims in published maps and institutional affiliations.

Methods

Cell culture. Unless otherwise specified, all cell lines (H460, 293 T, H292, RCC4, RCC4 + VHL, Gli56, D423, and NB-1) were cultured in DMEM (Gibco) with 10% FBS (Sigma). AML cell lines (KG1, THP1, MOLM13, K562, MV4-11, OCI-AML3, U937, Kasumi, and HL60) were cultured in RPMI (Gibco) with 5–20% FBS. D423 cells were provided by D. Bigner (Duncan et al.⁴⁸, Oncotarget 2010). Gli56 cells were provided by D. N. Louis (Mueller et al.⁴⁹, Oncogene 2005). NB-1 cells were obtained from the Japanese Cancer Research Resources Bank (JCRB) Cell Bank. All GSCs were kindly provided by F. Lang at MD Anderson Cancer Center (MDACC). GSCs were cultured in serum-free DMEM/F12 from American Type Culture Collection (ATCC) supplemented with 20 ng/ml basic fibroblast growth factor (bFGF) (Sigma), 20 ng/ml epidermal growth factor (EGF) (Sigma) and 1 × B27 supplement (Invitrogen). Normal diploid cells were purchased from ATCC and cultured following ATCC's guidelines. All other cell lines are from ATCC. RCC4 and RCC4VHL were obtained from European Collection of Authenticated Cell Cultures (ECACC). Cell lines were maintained at an internal core facility that routinely used short tandem repeat (STR) fingerprinting to verify cell line identity and performed mycoplasma testing to confirm they were negative.

Compound synthesis. *Step 1: synthesis of ethyl 3-(4-(trifluoromethoxy)phenyl)-1,2,4-oxadiazole-5-carboxylate.* To a solution of (*E*)-*N'*-hydroxy-4-(trifluoromethoxy)benzimidamide (Sigma-Aldrich, 60.0 g, 272 mmol) and pyridine (32.3 g, 408 mmol) in CHCl₃ (400 ml) at 0 °C was slowly added ethyl 2-chloro-2-oxoacetate (44.6 g, 327 mmol). The mixture was stirred at reflux for 3 h, cooled to RT and diluted with H₂O (400 ml). The mixture was extracted with dichloromethane (DCM, 400 ml × 2), the combined organic layers were washed with aqueous HCl (1 M, 300 ml × 2) and H₂O (400 ml), dried over Na₂SO₄, filtered, evaporated to give ethyl 3-(4-(trifluoromethoxy)phenyl)-1,2,4-oxadiazole-5-carboxylate as a light yellow solid (77.7 g, 94%), which was used for next step without further purification. Proton nuclear magnetic resonance (¹H NMR) (300 MHz, CDCl₃): δ 8.22 (d, *J* = 11.2 Hz, 2H), 7.36 (d, *J* = 11.2 Hz, 2H), 4.60 (q, *J* = 9.6 Hz, 2H), 1.51 (t, *J* = 9.6 Hz, 3H). ¹³C NMR (126 MHz, DMSO-*d*₆): δ 167.5, 167.1, 153.5, 150.7, 129.5, 124.4, 121.7, 119.9 (q, *J* = 257 Hz), 63.3, 13.7. ¹⁹F NMR (471 MHz, DMSO-*d*₆): δ -56.7. High-resolution mass spectrometry, electrospray ionization (HRMS, ESI⁺) *m/z*: [M + H]⁺ calculated for C₁₂H₁₀F₃N₂O₄, 303.0587; found, 303.0584.

Step 2: synthesis of 3-(4-(trifluoromethoxy)phenyl)-1,2,4-oxadiazole-5-carbohydrazide. To a solution of ethyl 3-(4-(trifluoromethoxy)phenyl)-1,2,4-oxadiazole-5-carboxylate (80.0 g, 265 mmol) in EtOH (800 ml) was added NH₂NH₂·H₂O (85%, 76.0 ml, 1,325 mmol). The reaction mixture was stirred at RT for 16 h. The desired compound precipitated from the reaction mixture and was filtered and washed with EtOH (200 ml) to produce 3-(4-(trifluoromethoxy)phenyl)-1,2,4-oxadiazole-5-carbohydrazide (70.2 g, 92%) as a light yellow solid, which was used for the next step without further purification. ¹H NMR (600 MHz, Methanol-*d*₄): δ 8.24 (d, *J* = 8.8 Hz, 2H), 7.47 (d, *J* = 8.6 Hz, 2H). ¹³C NMR (126 MHz, DMSO-*d*₆): δ 166.9, 129.4, 124.7, 121.7, 119.9 (q, *J* = 258 Hz). ¹⁹F NMR (471 MHz, DMSO-*d*₆): δ -56.6. HRMS (ESI⁺) *m/z*: [M + H]⁺ calculated for C₁₀H₈F₃N₃O₃, 289.0543; found, 289.0538.

Step 3: synthesis of 5-(5-methyl-1H-1,2,4-triazol-3-yl)-3-(4-(trifluoromethoxy)phenyl)-1,2,4-oxadiazole. NaOH (9.4 g, 234 mmol) was added to a mixture of 3-(4-(trifluoromethoxy)phenyl)-1,2,4-oxadiazole-5-carbohydrazide (45.0 g, 156 mmol) and aceticimidamide hydrochloride (22.2 g, 234 mmol) in tetrahydrofuran (THF) (500 ml). The mixture was refluxed for 3 d and then cooled to RT, concentrated under reduced pressure and diluted with H₂O (500 ml). The resulting suspension was stirred at RT for 30 min and then filtered to produce a crude solid product, which was treated with ethyl acetate (EtOAc) (400 ml). The resulting suspension was stirred at RT for 30 min and then filtered to produce 5-(5-methyl-1H-1,2,4-triazol-3-yl)-3-(4-(trifluoromethoxy)phenyl)-1,2,4-oxadiazole as a white solid (30.3 g, 62%). ¹H NMR (600 MHz, DMSO-*d*₆): δ 14.65 (s, 1H), 8.22 (d, *J* = 8.7 Hz, 2H), 7.61 (d, *J* = 8.6 Hz, 2H), 2.51 (s, 3H). ¹³C NMR (126 MHz, DMSO-*d*₆): δ 169.4, 167.2, 165.8, 155.3, 150.5, 129.4, 125.0, 121.7, 119.9 (q, *J* = 258 Hz), 11.5. ¹⁹F NMR (471 MHz, DMSO-*d*₆): δ -56.6. HRMS (ESI⁺) *m/z*: [M + H]⁺ calculated for C₁₂H₉F₃N₃O₃, 312.0703; found, 312.0699.

Step 4: synthesis of 5-(1-(3-bromobenzyl)-5-methyl-1H-1,2,4-triazol-3-yl)-3-(4-(trifluoromethoxy)phenyl)-1,2,4-oxadiazole. 1-bromo-3-(bromomethyl)benzene (48.2 g, 192.8 mmol) was added to a suspension of 5-(5-methyl-1H-1,2,4-triazol-3-yl)-3-(4-(trifluoromethoxy)phenyl)-1,2,4-oxadiazole (60.0 g, 192.8 mmol) and potassium carbonate (66.6 g, 482.0 mmol) in DMF (200 ml). The mixture was stirred at RT for 16 h and then diluted with water (500 ml) and extracted with EtOAc (3 × 500 ml). The combined organic layers were washed with H₂O (300 ml) and concentrated under reduced pressure to produce the crude product, which was purified using a silica gel chromatography column (eluent: 4:1 to 3:2, petroleum ether (PE):EtOAc) to produce 5-(1-(3-bromobenzyl)-5-methyl-1H-1,2,4-triazol-3-yl)-3-(4-(trifluoromethoxy)phenyl)-1,2,4-oxadiazole as a white solid (53.6 g, 57.9%). ¹H NMR (600 MHz, CDCl₃): δ 8.28 (d, *J* = 8.8 Hz, 2H), 7.48 (d, *J* = 7.9 Hz, 1H), 7.41 (s, 1H), 7.34 (d, *J* = 8.8 Hz, 2H), 7.26 (d, *J* = 7.6 Hz, 1H), 7.17 (d, *J* = 7.9 Hz, 1H), 5.43 (s, 2H), 2.55 (s, 3H). ¹³C NMR (126 MHz, DMSO-*d*₆): δ 168.9, 167.2, 155.4, 150.5, 148.2, 137.8, 131.0, 131.0, 130.5,

129.4, 126.9, 124.9, 121.9, 121.6, 119.9 (q, *J* = 258 Hz), 51.1, 11.6. ¹⁹F NMR (471 MHz, DMSO-*d*₆): δ -56.6. HRMS (ESI⁺) *m/z*: [M + H]⁺ calculated for C₁₉H₁₄BrF₃N₃O₂, 480.0277, 482.0257; found 480.0270, 480.0247.

Step 5: synthesis of IACS-010759 5-(5-methyl-1-(3-(4-(methylsulfonyl)piperidin-1-yl)benzyl)-1H-1,2,4-triazol-3-yl)-3-(4-(trifluoromethoxy)phenyl)-1,2,4-oxadiazole. 2-dicyclohexylphosphino-2,6'-di-*i*-propoxy-1,1'-biphenyl (580 mg, 1.25 mmol) and tris(dibenzylideneacetone)dipalladium (760 mg, 0.83 mmol) were added to a mixture of 5-(1-(3-bromobenzyl)-5-methyl-1H-1,2,4-triazol-3-yl)-3-(4-(trifluoromethoxy)phenyl)-1,2,4-oxadiazole (2.00 g, 4.16 mmol), 4-(methylsulfonyl)piperidine (1.02 mg, 6.24 mmol), and *t*-BuONa (800 mg, 8.33 mmol) in toluene (80 ml), and the reaction mixture was degassed with argon for 3 min and then was heated to 140 °C for 18 h under an argon atmosphere. The mixture was then cooled to RT, diluted with EtOAc (100 ml), filtered through a pad of celite, washed with EtOAc (100 ml), and concentrated under reduced pressure. The residue was purified using a silica gel chromatography column (PE:EtOAc = 1:1 with pure EtOAc) to produce a crude product, which was treated with EtOAc and Et₂O (vol/vol = 1:9, 30 ml). The resulting suspension was stirred at RT for 30 min and then filtered to produce 5-(5-methyl-1-(3-(4-(methylsulfonyl)piperidin-1-yl)benzyl)-1H-1,2,4-triazol-3-yl)-3-(4-(trifluoromethoxy)phenyl)-1,2,4-oxadiazole as a white solid (905 mg, 39%). ¹H NMR (600 MHz, DMSO-*d*₆): δ 8.22 (d, *J* = 8.8 Hz, 2H), 7.61 (d, *J* = 8.2 Hz, 2H), 7.21 (t, *J* = 7.9 Hz, 1H), 6.97 (bs, 1H), 6.94 (dd, *J* = 8.3, 2.4 Hz, 1H), 6.64 (d, *J* = 7.5 Hz, 1H), 5.48 (s, 2H), 3.86 (bd, *J* = 13.4 Hz, 2H), 3.28 (m, 1H), 2.94 (s, 3H), 2.76 (m, 2H), 2.57 (s, 3H), 2.06 (bd, *J* = 13.4 Hz, 2H), 1.68 (ddd, *J* = 16.5, 12.5, 4.1 Hz, 2H). ¹³C NMR (126 MHz, DMSO-*d*₆): δ 169.0, 167.2, 155.1, 150.7, 150.5, 147.9, 136.0, 129.6, 129.6, 129.4, 124.9, 121.7, 119.9 (q, *J* = 258 Hz), 117.8, 115.5, 115.2, 58.6, 52.3, 47.2, 37.4, 23.7, 11.7. ¹⁹F NMR (471 MHz, DMSO-*d*₆): δ -56.6. HRMS (ESI⁺) *m/z*: [M + H]⁺ calculated for C₂₅H₂₆F₃N₆O₄S, 563.1683; found, 563.1675.

Oxygen consumption. AML cells were suspended normal growth medium at a concentration of 1 × 10⁷ cells/ml, and 100 μl of cells was added to Seahorse 96-well plates pre-coated with Cell-Tak. Plates were centrifuged at 1,000 r.p.m., and medium was replaced with prewarmed (37 °C) 125 μl Seahorse medium (Seahorse XF medium with 2 mM glutamax, 10 mM glucose, 2 mM pyruvate) containing IACS-010759 or rotenone (41 nM). For AML cell lines, 3 × 10⁵ total cells were seeded per well in Seahorse XF medium with 2 mM glutamine, 10 mM glucose, and 2 mM pyruvate. The mitostress test was performed with 1 μM oligomycin, 0.4–1 μM FCCP, and 1 μM antimycin. For oxygen consumption in permeabilized tumor cells (Fig. 1d), H460 cells were suspended in Seahorse XF assay medium and plated at a concentration of 15 × 10³ cells/well of Seahorse 96-well plates pre-coated with Cell-Tak. Plates were centrifuged at 1,000 r.p.m., and medium was replaced with prewarmed (37 °C) 100 μl of 10 mM pyruvate and 2 mM malate substrate + 4 μM FCCP (uncoupled) in the 1 × Mitochondria Assay Solution (MAS) medium. Immediately before IACS-010759 injection, plasma membrane permeabilizer (PMP) was added to a final concentration of 1 nM, and ADP was added to a final concentration of 4 nM. Final drug and substrate concentrations were 10, 100, or 1,000 nM for IACS-010759; 100 nM for rotenone; 10 mM for succinate; 4 μM for antimycin. A detailed protocol is provided by Agilent at <https://www.agilent.com/cs/library/usermanuals/public/insert-xf-pmp-reagent-web.pdf>.

Seahorse analyses for AML cell lines and the patient-derived xenograft (PDX) model were performed according to Seahorse Biosciences protocol for the mitostress test. Briefly, 300,000 cells per well were seeded in 175 μl of Seahorse XF medium supplemented with 10 mM glucose, 2 mM glutamine, and 1 mM pyruvate. FCCP concentration was optimized for each cell line model (1.6–0.2 μM), and data were normalized to cell number.

Seahorse analyses for basal OCAR and ECAR were performed using reagents from Seahorse Bioscience, as previously reported³⁰.

Ectopic expression of NDI-1. HEK293T cells were transfected with pCMV-dR8.9 packaging DNA vector, pMD2.G VSV-G-expressing envelope vector, and pLenti6.3 NDI-1, pLenti6.3/V5 NDI-1, or pLenti6.3/V5 GFP plasmid DNA. 2 × 10⁵ H460 cells were transfected in a 6-well plate with 2 ml of viral supernatant supplemented with polybrene to a final concentration of 8 μg/ml. After infection, transduced cells were selected through growth in 7 μg/ml blasticidin. The concentration of IACS-010759 used in the graph in Fig. 1e was 14 nM.

Isolated mouse complex I assay. Complex I was isolated from mouse heart mitochondria using an adaptation of the method of Sharpley and colleagues⁵¹. The concentration of IACS-010759 in Fig. 1f was 60 nM. The NADH:deacylubiquinone assay is described in Sharpley et al.⁵², and the APAD⁺ and H₂O₂ assays are described in Birrell et al.⁵².

Generation of clonal cell lines resistant to IACS-010759. H292 cells (1 × 10⁶ cells/plate) were seeded in 15-cm dishes in galactose growth medium and treated with 1 nM IACS-010759 (IC₆₅) for 3 weeks, followed by exposure to 8 nM IACS-010759 (IC₆₅) until resistant clones emerged. Twenty-six resistant clones were isolated from four independent experiments and were seeded at 5 × 10³ cells/well in 96-well plates in 100 μl galactose growth medium. After cells became fully attached,

IACS-010759 or rotenone was added to a final concentration of 370 nM to 18 pM for 3 d. Plates were scanned in the IncuCyte live-cell analysis system before analysis via Hoechst and PI. Subsequently, both Hoechst and PI using an Operetta high-content imaging system. RNA-seq was conducted on the parental line and 12 resistant clones, uncovering a single nonsynonymous, heteroplasmic (35–50%), recurrent mutation in the mitochondrial-encoded gene *MT-ND1* in 9 of the 12 resistant clones that conferred the L55F (T3469C) amino acid change. Paired-end reads were initially aligned to transcript sequences of complex I genes with Bowtie 2 (ref.⁵³), and the aligned fragments were probabilistically assigned to transcripts using eXpress⁵⁴. Variants from the reference genome were called using the 'mpileup' command in SAMtools. MutPred⁵⁵ analysis of the L55F variant classifies the alteration as potentially pathogenic (MutPred score = 0.8); this alteration is found at a very low frequency in mtDNA sequences in Genebank (1:30,589 based on full-length mitochondrial genomes deposited in Genebank before 28 October 2015), suggesting it is unlikely to be a polymorphism. The mutation was confirmed in four of the resistant clones by cloning the MT-ND1 gene sequence (ZERO blunt PCR; Invitrogen) and analyzing purified plasmid DNA via Sanger sequencing using the following primers: Forward: 5'-GTAACGACGCGCCAGT-3' and Reverse: 5'-AACAGCTATGACCATG-3'.

Metabolomics for glycolysis-deficient models. NB-1, D423, Gli56, A1207, SW1088, and U87 were plated and treated with DMSO or 100 nM IACS-010759 in a 10-cm plate. Two days after, the cells were briefly washed in cold PBS, scrapped in 80% methanol, and spun down. The supernatant was dried in a GeneVac HT4 using the low-temperature program (SP Scientific). The dried samples were resuspended and subjected to a liquid chromatography and mass spectrometry (LC–MS) analysis that covers over 200 metabolites by J. M. Asara's group at Beth Israel Deaconess Medical Center, as previously described⁵⁶. Analysis of metabolite peak area integrated total ion chromatogram values was carried out using the statistical computing language R. Metabolites with missing data in any sample were excluded, and the remaining values were quantile normalized. Statistical comparisons of groups was performed with limma, and all *P* values were reported corrected for multiple-hypothesis testing using the Benjamini–Hochberg method.

LC–MS for targeted metabolomics and stable-isotope tracing in AML cell lines.

For targeted metabolomics, dried cellular extracts from OCI-AML3 cultures were reconstituted with 1:1 acetonitrile:water (40 µl), and aliquots (5 µl) were analyzed on an Agilent 1290 ultra-high performance liquid chromatography (UHPLC) system coupled with an Agilent 6550 quadrupole-time of flight (Q-TOF) mass spectrometer operating in negative ion mode. Details about LC–MS analysis conditions are reported in Appendix 1. Acquired Q-TOF raw data were processed using Agilent MassHunter Profinder 8.0 software, and target metabolites were identified using the built-in batch-targeted feature extraction algorithm, which used an in-house accurate mass-retention time (AMRT) database library, including 126 endogenous metabolites. Identified compound signal intensities were extracted and subjected to statistical analysis in Agilent Mass Profiler Professional (MPP). Sample metabolite raw abundancies were log₂ transformed, normalized by their correspondent sample protein content or viable cell count, and centered to their median signal intensities. The unpaired Welch's *t*-test was used to determine statistically significant variations across sample groups (for detailed methodology, refer to Supplementary Methods).

For stable-isotope tracing experiments, samples for LC–MS analysis were prepared as described above and analyzed on an Agilent 6550 Q-TOF. The raw data were analyzed in MassHunter Profinder 8.0 by running the batch isotopologue extraction algorithm against an accurate mass retention time (AMRT) in-house compound library including the compounds of interest. The resulting isotopologue abundancies were corrected for their isotopic natural abundance, extracted as detailed CVS files, and tested for significant variations using a Welch's *t*-test. Details about cell growth and LC–MS analysis are reported in Appendix 1 (for detailed methodology, refer to Appendix 1).

Primary AML cells and normal bone marrow. Peripheral blood samples from patients with AML were collected during routine diagnostic procedures after informed consent was obtained in accordance with the regulations and protocols (LAB 01-473) approved by the MDACC Investigational Review Board (IRB) in accordance with IRB regulations of The University of Texas MD Anderson Cancer Center and the Declaration of Helsinki. AML samples were analyzed under the IRB-approved laboratory protocol PA13-1025. Briefly, mononuclear cells were separated by Ficoll–Hypaque density gradient centrifugation and incubated in RBC lysis buffer (ammonium chloride solution) to remove red blood cells. Primary leukemia samples were maintained in StemEZ Serum-Free Medium. Viability and induction of apoptosis were assessed simultaneously using flow cytometry. 1 to 3 million cells were grown in triplicate in 24-well plates and exposed to DMSO or IACS-010759. Cells were harvested after 3, 4, or 5 d of exposure to agent and were resuspended in binding buffer containing Annexin V. Apoptotic cells were detected by Annexin V flow cytometry after gating on CD45⁺ leukemic cells. Viable cells were detected by flow cytometry with anti-human CD45-FITC antibody (BD Pharmingen) staining after exclusion of nonviable cells determined with DAPI staining (Sigma-Aldrich) and apoptotic cells. Flow cytometry was performed

on Gallios Flow Cytometer, and data were analyzed using Kaluza Flow Analysis software (Beckman Coulter). For normal bone marrow, the same procedure was followed.

Gene expression signature. To determine whether specific gene pathways were altered by treatment with IACS-010759, REACTOME pathway analysis was performed on the genes that were significantly upregulated (132 genes) or downregulated (132 genes) in > 2 cell lines following 24-h treatment with 100 nM IACS-010759. The top four gene pathways upregulated in response to IACS-010759 were all related to amino acid biosynthesis (Supplementary Fig. 13a), consistent with the finding that metabolite levels are altered in response to IACS-010759 described above. The fifth upregulated pathway included genes regulated by ATF4, which is a transcription factor that upregulates genes that deal with cellular stress in response to decreased amino acids and energy intermediates. The top five downregulated pathways all involve genes involved in cell cycle progression (Supplementary Fig. 13b).

Genes whose expression was modulated by treatment with IACS-010759 in > 3 cell lines were selected for validation in vivo with a custom NanoString codeset. Samples from an acute pharmacokinetics and pharmacodynamics (PK/PD) study conducted in a primary patient-derived xenograft mouse model of AML were harvested in triplicate after 48 h of treatment with 1, 2.5, or 7.5 mg/kg IACS-010759 and in duplicate for vehicle treatment. Analysis of NanoString data was carried out using the statistical computing language R. Normalization factors were calculated on the basis of the internal positive controls and a selected set of housekeeping genes (*CLTC*, *TBP*, *ALAS1*, *ACTB*, and *RPL19*) according to the nCounter Expression Data Analysis Guide. For each sample, to control for variability in hybridization across samples, the geometric mean of the internal controls was calculated and then used to normalize across samples. To control for variability associated with the amount of input mRNA, the geometric mean of the housekeeping genes was calculated and then used to normalize samples for the amount of input mRNA. Data were normalized to vehicle samples, and genes were ranked by the magnitude of alteration at the highest dose (Supplementary Fig. 8c). A subset of genes were dose-dependently downregulated upon treatment, with a more than twofold decrease in expression at the highest dose of IACS-010759 (Supplementary Fig. 13c–e). Variability in mRNA signal for each gene was minimal across the three mice within a dosing group.

The top-scoring gene was *IL8*, and it was equally inhibited at all three dose levels (Supplementary Figs. 13d,e). In contrast, other genes showed a dose-dependent inhibition over this range (Supplementary Figs. 13d,e). A 'summary score' was constructed on the basis of the average fold change of the 12 genes for which the highest dose-dependent downregulation was observed in response to IACS-010759 (*RRM2*, *HMG2*, *DHCR24*, *PCNA*, *KIF11*, *TK1*, *KLGA25*, *KIF20A*, *CDCA5*, *CCNB1*, and *FEN1*) and plotted against plasma levels for the PK/PD analysis shown in Supplementary Fig. 13f. This analysis shows a dose-dependent decrease in expression of this group of genes in response to IACS-010759 treatment.

Reporting Summary. Further information on experimental design is available in the Nature Research Reporting Summary linked to this article.

Data availability. All data supporting this study are available from the corresponding author upon reasonable request.

References

- Duncan, D. C. et al. Integrated genomic analyses identify *ERRF1* and *TACC3* as glioblastoma-targeted genes. *Oncotarget* **1**, 265–277 (2010).
- Mueller, W. et al. Downregulation of *RUNX3* and *TES* by hypermethylation in glioblastoma. *Oncogene* **26**, 583–593 (2005).
- Sun, Y. et al. Metabolic and transcriptional profiling reveals pyruvate dehydrogenase kinase 4 as a mediator of epithelial-mesenchymal transition and drug resistance in tumor cells. *Cancer Metab.* **2**, 20 (2014).
- Sharpley, M. S., Shannon, R. J., Draghi, F. & Hirst, J. Interactions between phospholipids and NADH:ubiquinone oxidoreductase (complex I) from bovine mitochondria. *Biochemistry* **45**, 241–248 (2006).
- Birrell, J. A., Yakovlev, G. & Hirst, J. Reactions of the flavin mononucleotide in complex I: a combined mechanism describes NADH oxidation coupled to the reduction of APAD⁺, ferricyanide, or molecular oxygen. *Biochemistry* **48**, 12005–12013 (2009).
- Langmead, B. & Salzberg, S. L. Fast gapped-read alignment with Bowtie 2. *Nat. Methods* **9**, 357–359 (2012).
- Roberts, A. & Pachter, L. Streaming fragment assignment for real-time analysis of sequencing experiments. *Nat. Methods* **10**, 71–73 (2013).
- Li, B. et al. Automated inference of molecular mechanisms of disease from amino acid substitutions. *Bioinformatics* **25**, 2744–2750 (2009).
- Yuan, M., Breitkopf, S. B., Yang, X. & Asara, J. M. A positive/negative ion-switching, targeted mass spectrometry-based metabolomics platform for bodily fluids, cells, and fresh and fixed tissue. *Nat. Protoc.* **7**, 872–881 (2012).

Reporting Summary

Nature Research wishes to improve the reproducibility of the work that we publish. This form provides structure for consistency and transparency in reporting. For further information on Nature Research policies, see [Authors & Referees](#) and the [Editorial Policy Checklist](#).

Statistical parameters

When statistical analyses are reported, confirm that the following items are present in the relevant location (e.g. figure legend, table legend, main text, or Methods section).

n/a Confirmed

- The exact sample size (n) for each experimental group/condition, given as a discrete number and unit of measurement
- An indication of whether measurements were taken from distinct samples or whether the same sample was measured repeatedly
- The statistical test(s) used AND whether they are one- or two-sided
Only common tests should be described solely by name; describe more complex techniques in the Methods section.
- A description of all covariates tested
- A description of any assumptions or corrections, such as tests of normality and adjustment for multiple comparisons
- A full description of the statistics including central tendency (e.g. means) or other basic estimates (e.g. regression coefficient) AND variation (e.g. standard deviation) or associated estimates of uncertainty (e.g. confidence intervals)
- For null hypothesis testing, the test statistic (e.g. F , t , r) with confidence intervals, effect sizes, degrees of freedom and P value noted
Give P values as exact values whenever suitable.
- For Bayesian analysis, information on the choice of priors and Markov chain Monte Carlo settings
- For hierarchical and complex designs, identification of the appropriate level for tests and full reporting of outcomes
- Estimates of effect sizes (e.g. Cohen's d , Pearson's r), indicating how they were calculated
- Clearly defined error bars
State explicitly what error bars represent (e.g. SD, SE, CI)

Our web collection on [statistics for biologists](#) may be useful.

Software and code

Policy information about [availability of computer code](#)

Data collection

Data analysis

For manuscripts utilizing custom algorithms or software that are central to the research but not yet described in published literature, software must be made available to editors/reviewers upon request. We strongly encourage code deposition in a community repository (e.g. GitHub). See the Nature Research [guidelines for submitting code & software](#) for further information.

Data

Policy information about [availability of data](#)

All manuscripts must include a [data availability statement](#). This statement should provide the following information, where applicable:

- Accession codes, unique identifiers, or web links for publicly available datasets
- A list of figures that have associated raw data
- A description of any restrictions on data availability

Included "The authors declare that the data supporting the findings of this study are available within the paper and its supplementary information files."

Field-specific reporting

Please select the best fit for your research. If you are not sure, read the appropriate sections before making your selection.

Life sciences Behavioural & social sciences

For a reference copy of the document with all sections, see [nature.com/authors/policies/ReportingSummary-flat.pdf](https://www.nature.com/authors/policies/ReportingSummary-flat.pdf)

Life sciences

Study design

All studies must disclose on these points even when the disclosure is negative.

Sample size	Included in final text.
Data exclusions	Included where applicable.
Replication	All experiments included multiple independent samples and in most experiments were repeated multiple times with comparable results. Additional independent studies were repeated using identical or similar conditions and reagents to ensure the results were reproducible and representative.
Randomization	Included in text.
Blinding	Where appropriate, the researcher was blinded to the identity of the material and noted in the methods.

Materials & experimental systems

Policy information about [availability of materials](#)

n/a	Included in the study
<input type="checkbox"/>	<input checked="" type="checkbox"/> Unique materials
<input type="checkbox"/>	<input checked="" type="checkbox"/> Antibodies
<input type="checkbox"/>	<input checked="" type="checkbox"/> Eukaryotic cell lines
<input type="checkbox"/>	<input checked="" type="checkbox"/> Research animals
<input type="checkbox"/>	<input checked="" type="checkbox"/> Human research participants

Unique materials

Obtaining unique materials	No restrictions where possible to share.
----------------------------	--

Antibodies

Antibodies used	Included.
Validation	All were validated internally or externally.

Eukaryotic cell lines

Policy information about [cell lines](#)

Cell line source(s)	Included in text.
Authentication	Included in text.
Mycoplasma contamination	All cell lines were tested and confirmed to be negative for mycoplasma.
Commonly misidentified lines (See ICLAC register)	None used.

Research animals

Policy information about [studies involving animals](#); [ARRIVE guidelines](#) recommended for reporting animal research

Animals/animal-derived materials	Included in text.
----------------------------------	-------------------

Human research participants

Policy information about [studies involving human research participants](#)Population characteristics

Method-specific reporting

- | | |
|-------------------------------------|---|
| n/a | <input checked="" type="checkbox"/> Involved in the study |
| <input checked="" type="checkbox"/> | <input type="checkbox"/> ChIP-seq |
| <input type="checkbox"/> | <input checked="" type="checkbox"/> Flow cytometry |
| <input checked="" type="checkbox"/> | <input type="checkbox"/> Magnetic resonance imaging |

Flow Cytometry

Plots

Confirm that:

- The axis labels state the marker and fluorochrome used (e.g. CD4-FITC).
- The axis scales are clearly visible. Include numbers along axes only for bottom left plot of group (a 'group' is an analysis of identical markers).
- All plots are contour plots with outliers or pseudocolor plots.
- A numerical value for number of cells or percentage (with statistics) is provided.

Methodology

Sample preparation Instrument Software Cell population abundance Gating strategy

- Tick this box to confirm that a figure exemplifying the gating strategy is provided in the Supplementary Information.